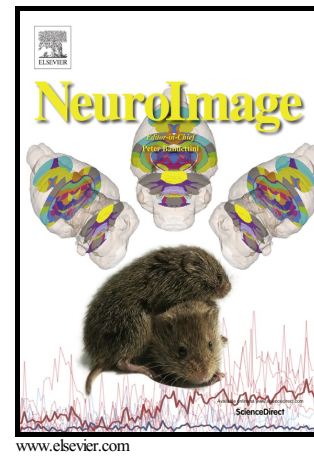


## Author's Accepted Manuscript

Manual segmentation of the fornix, fimbria, and alveus on high-resolution 3T MRI: Application via fully-automated mapping of the human memory circuit white and grey matter in healthy and pathological aging

Robert S.C. Amaral, Min Tae M. Park, Gabriel A. Devenyi, Vivian Lynn, Jon Pipitone, Julie Winterburn, Sofia Chavez, Mark Schira, Nancy Lobaugh, Aristotle N. Voineskos, Jens C. Pruessner, M. Mallar Chakravarty



PII: S1053-8119(16)30581-X  
DOI: <http://dx.doi.org/10.1016/j.neuroimage.2016.10.027>  
Reference: YNIMG13524

To appear in: *NeuroImage*

Received date: 7 April 2016  
Revised date: 14 October 2016  
Accepted date: 17 October 2016

Cite this article as: Robert S.C. Amaral, Min Tae M. Park, Gabriel A. Devenyi, Vivian Lynn, Jon Pipitone, Julie Winterburn, Sofia Chavez, Mark Schira, Nancy Lobaugh, Aristotle N. Voineskos, Jens C. Pruessner and M. Mallar Chakravarty, Manual segmentation of the fornix, fimbria, and alveus on high-resolution 3T MRI: Application via fully-automated mapping of the human memory circuit white and grey matter in healthy and pathological aging, *NeuroImage* <http://dx.doi.org/10.1016/j.neuroimage.2016.10.027>

This is a PDF file of an unedited manuscript that has been accepted for publication. As a service to our customers we are providing this early version of the manuscript. The manuscript will undergo copyediting, typesetting, and a review of the resulting galley proof before it is published in its final citable form. Please note that during the production process errors may be discovered which could affect the content, and all legal disclaimers that apply to the journal pertain.

SUBMISSION TO: *NEUROIMAGE* special issue, *Brain Segmentation and Parcellation*

## **Manual segmentation of the fornix, fimbria, and alveus on high-resolution 3T MRI: Application via fully-automated mapping of the human memory circuit white and grey matter in healthy and pathological aging**

Robert S.C. Amaral<sup>1,2</sup>, Min Tae M. Park<sup>1,3</sup>, Gabriel A. Devenyi<sup>1</sup>, Vivian Lynn<sup>1</sup>, Jon Pipitone<sup>4</sup>, Julie Winterburn<sup>1,5</sup>, Sofia Chavez<sup>6,7</sup>, Mark Schira<sup>8,9</sup>, Nancy Lobaugh<sup>7,10</sup>, Aristotle N. Voineskos<sup>4,6</sup>, Jens C. Pruessner<sup>11</sup>, M. Mallar Chakravarty<sup>1,2,12,13</sup>, the Alzheimer's Disease Neuroimaging Initiative\*

<sup>1</sup> Computational Brain Anatomy Laboratory, Cerebral Imaging Centre, Douglas Mental Health University Institute, Montreal, Canada

<sup>2</sup> Integrated Program in Neuroscience, McGill University, Montreal, Canada

<sup>3</sup> Schulich School of Medicine and Dentistry, Western University, London, Canada

<sup>4</sup> Kimel Family Translational Imaging-Genetics Laboratory, Campbell Family Mental Health Institute, CAMH, Toronto, Canada

<sup>5</sup> Institute of Biomaterials and Biomedical Engineering, University of Toronto, Canada

<sup>6</sup> Department of Psychiatry, University of Toronto, Toronto, Canada

<sup>7</sup> MRI Unit, Research Imaging Centre, Centre for Addiction and Mental Health, Toronto, Canada

<sup>8</sup> School of Psychology, University of Wollongong, Wollongong, NSW, Australia

<sup>9</sup> Neuroscience Research Australia, Sydney, NSW, Australia

<sup>10</sup> Division of Neurology, Department of Medicine, University of Toronto, Toronto, Canada

<sup>11</sup> McGill Centre for Studies in Aging, McGill University, Montreal, Canada

<sup>12</sup> Department of Psychiatry, McGill University, Montreal, Canada

<sup>13</sup> Department of Biological and Biomedical Engineering, McGill University, Montreal, Canada

Corresponding Authors: Robert S.C. Amaral & Dr. M. Mallar Chakravarty

Address: 6875 Boulevard LaSalle  
Verdun, QC, Canada  
H4H 1R3

TEL.: (514) 761-6131 Ext.: 4753

FAX: (514) 888-4487

EMAIL: robert.amaral@mail.mcgill.ca  
mallar@cobralab.ca

Running title: Manual and automatic segmentation of the fornix, fimbria, and alveus

\*Data used in preparation of this article were obtained from the Alzheimer's Disease Neuroimaging Initiative (ADNI) database (adni.loni.usc.edu). As such, the investigators within the ADNI contributed to the design and implementation of ADNI and/or provided data but did not participate in analysis or writing of this report. A complete listing of ADNI investigators can be found at: [http://adni.loni.usc.edu/wp-content/uploads/how\\_to\\_apply/ADNI\\_Acknowledgement\\_List.pdf](http://adni.loni.usc.edu/wp-content/uploads/how_to_apply/ADNI_Acknowledgement_List.pdf).

## ABSTRACT

Recently, much attention has been focused on the definition and structure of the hippocampus and its subfields, while the projections from the hippocampus have been relatively understudied. Here, we derive a reliable protocol for manual segmentation of hippocampal white matter regions (alveus, fimbria, and fornix) using high-resolution magnetic resonance images that are complementary to our previous definitions of the hippocampal subfields, both of which are freely available at <http://cobralab.net/files/AmaralWhitematterAtlas.zip>. Our segmentation methods demonstrated high inter- and intra-rater reliability, were validated as inputs in automated segmentation, and were used to analyze the trajectory of these regions in both healthy aging (OASIS), and Alzheimer's disease (AD) and mild cognitive impairment (MCI; using ADNI). We observed significant bilateral decreases in the fornix in healthy aging while the alveus and cornu ammonis (CA) 1 were well preserved (all  $p$ 's < 0.006). MCI and AD demonstrated significant decreases in fimbriae and fornices. Many hippocampal subfields exhibited decreased volume in both MCI and AD, yet no significant differences were found between MCI and AD cohorts themselves. Our results suggest a neuroprotective or compensatory role for the alveus and CA1 in healthy aging and suggest that an improved understanding of the volumetric trajectories of these structures is required.

KEYWORDS: Anatomy, AD, Hippocampus, MCI, Tracing, White Matter

## 1.0 INTRODUCTION

In recent years the human hippocampus and medial temporal lobe (MTL) cortices have

received considerable attention in the study of health and disease. Among the many cognitive processes that involve these structures, their vital role within the memory circuit has been, for the most part, well documented (see Eichenbaum, Yonelinas, & Ranganath, 2007 for review). Located in the MTL, the circuit involves the projection of sensory inputs to the MTL cortices (i.e. the perirhinal, parahippocampal, and entorhinal cortices), which then direct inputs to the hippocampus (Amaral & Lavenex, 2007; Duvernoy, Cattin, & Risold, 2013). The neuroanatomical subdivisions of the hippocampus include several subfields with intricate morphology and complex synaptic connections. Although terminology varies across authors, the most consistently recognized subfields that together define the hippocampal formation (HF) include: the subiculum, cornu ammonis (CA; 1 to 4) and the dentate gyrus (DG; Duvernoy et al., 2013; Konrad et al., 2009). Although some authors include the presubiculum, parasubiculum and entorhinal cortex (Andersen, 2007; Witter, 2007), the present paper maintains the subfields in the aforementioned definition of HF.

While controversy exists regarding the structure-function relationships of the subfields, there is general consensus that subfields play an important role in the encoding and translational process of memory formation (e.g. Lee, Rao, & Knierim, 2004; Mueller, Chao, Berman, & Weiner, 2011). The constantly improving resolution and contrast of magnetic resonance imaging (MRI) acquisition and analysis techniques has motivated an increasing number of researchers to study the structure and function of HF subfields. For example, both the MTL cortices and HF subfields have been relatively well-studied within the context of neurodegenerative disease states (Apostolova & Thompson, 2008; Chételat et al., 2008; Frisoni et al., 2008) as well as healthy aging (Voineskos et al., 2015; La Joie et al., 2010; Mueller & Weiner, 2009; Mueller et al., 2007). However, throughout the majority of its anterior to posterior extent, the HF is enveloped on its superior surface by white matter (WM) emanating from within the HF. These afferent myelinated fibers coat the HF (i.e. alveus and fimbria) and contour its trajectory through the MTL

(see SM Figure 1). Near the HF tail, the WM coalesces while curving superiorly and anteriorly forming the fornix. Projections then reach the anterior nuclei of the thalamus via the mammillary bodies prior to their ascent into higher cortical regions. It is these WM regions that have received significantly less attention in the literature.

Recent *in vivo* structural MRI of the HF and its subfields have utilized a combination of high-field and high-resolution MRI acquisition techniques, post-mortem data, and long scan times to image HF subfields (Adler et al., 2014; La Joie et al., 2010; Mueller et al., 2007; Olsen et al., 2013; Palombo et al., 2013; Van Leemput et al., 2009; Winterburn et al., 2013; Wisse et al., 2012; Yushkevich et al., 2009). An important limitation is the laborious manual segmentation for deriving the definitions of different subfields, although, some fully automated algorithms do exist (Iglesias et al., 2015; Pipitone et al., 2014; Van Leemput et al., 2009; Yushkevich, Pluta, et al., 2015b; Yushkevich et al., 2010). While, several protocols exist for segmentation of HF subfields (La Joie et al., 2010; Mueller et al., 2007; Olsen et al., 2013; Palombo et al., 2013; Van Leemput et al., 2009; Winterburn et al., 2013) and the MTL cortices (Olsen et al., 2013; Palombo et al., 2013; Pruessner et al., 2002), few exist for the WM regions of the memory circuit.

Previously published protocols for the segmentation of the fornix (see: Bilir et al., 1998; Copenhaver et al., 2006; Gale, Johnson, Bigler, & Blatter, 1995; Kuzniecky et al., 1999; Zahajszky et al., 2001) have several limitations: they exclude the posterior and/or anterior areas of the fornix, they do not separate the left and right fornices, and they use standard MRI acquisitions that are limited in resolution and contrast. Most protocols, because of limitations in image resolution, excluded the alveus and fimbria altogether. Although some groups have completed segmentations of the alveus and fimbria as part of HF subfield work (Parekh, Rutt, Purcell, Chen, & Zeineh, 2015; Wang et al., 2003; Zeineh, Holdsworth, Skare, Atlas, & Bammer, 2012), protocols often lack anatomical details (partly due to limited resolution), and tend to group

the alveus and fimbria together. Although such grouping serves to instill a more reliable WM definition, this introduces structural inaccuracies and limits the depth of investigation possible.

Given the absence of a viable segmentation protocol for the alveus, fimbria and fornix, our first objective was to create a complete, detailed, and reliable segmentation procedure adhering to the true anatomy of these regions. The resulting segmentation protocol maps the complete anterior–posterior extent of the alveus, fimbria, and fornix using high-resolution 3T MRI-data previously used to define HF subfield anatomy and complements our previous protocol for HF subfield segmentation (Winterburn et al., 2013). In addition, we have made these atlases freely available for use by the scientific community at <http://cobralab.net/files/AmaralWhitematterAtlas.zip>. Our second objective was to evaluate the automatic labeling of these structures on standard MRI data using a framework validated previously for labeling HF subfields (Chakravarty et al., 2013; Pipitone et al., 2014). Our third objective was to characterize the volume of the HF and WM substructures through the course of healthy and pathological aging using these newly derived atlases of the HF subfields and WM tracts as inputs. Specifically, the OASIS dataset (416 individuals aged 18-96; Marcus et al., 2007) was used to investigate the normative trends of HF and WM substructure through the course of healthy aging. Lastly, we explored the volumetry of these WM structures in the study of patients suffering from Alzheimer’s disease (AD) or mild cognitive impairment (MCI) using data from the Alzheimer’s NeuroImaging Initiative (ADNI1) 3T baseline dataset. We hypothesized there would be a decrease in all WM volumes throughout aging and across MCI and AD conditions relative to controls. Specifically, we hypothesized stepwise decreases in WM regions, with the AD cohort exhibiting the greatest WM volume loss relative to the control group.

## **2.0 METHODS**

Three main methods were used to produce the contributions of this manuscript. The first involves the description of the detailed manual segmentation protocol defined for the WM

(alveus, fimbria, and fornix) of the HF; the second is the validation of this protocol for use in a fully automated segmentation scheme; and the final is the application of the automated protocol on the OASIS and ADNI datasets to study healthy and pathological aging respectively.

## 2.1 Atlas Image Acquisition

Acquisition and pre-processing protocols have been described previously in detail (Park et al., 2014; Winterburn et al., 2013) but are repeated here for thoroughness. High-resolution T1- and T2-weighted images used for the development of our manual segmentation protocol are from data acquired from 5 healthy subjects (2 male, 3 female, aged 29-57, average age of 37 years). All images were acquired on a 3T GE Discovery MR 750 system (General Electric, Milwaukee, WI) at the Centre for Addiction and Mental Health (Toronto, Canada) using an 8-channel head coil. Three separate sets of high-resolution T1 and T2-weighted images were acquired. T1-weighted images were acquired using the 3D inversion-prepared fast spoiled gradient-recalled echo acquisition (FSPGR-BRAVO; TE/TR = 4.3 ms/9.2 ms, TI = 650 ms,  $\alpha = 8^\circ$ , 2NEX, FOV = 22 cm, slice thickness = 0.6 mm,  $384 \times 384$  in-plane steps). High-resolution T2-weighted images were acquired using the 3D fast spin echo acquisition (FSE-CUBE; TE/TR = 95.3 ms/2500 ms, ETL = 100 ms, 2NEX, FOV = 22 cm, slice thickness = 0.6 mm,  $384 \times 384$  in-plane steps). Both image sets have an isotropic voxel size of 0.6 mm. A final isotropic voxel size of 0.3 mm was obtained for both T1 and T2 images using reconstruction filters, ZIPX2 and ZIP512. All images were converted to the MINC file format and subsequent image processing and neuroanatomical labeling was performed using tools from the MINC software distribution (<http://www.bic.mni.mcgill.ca/ServicesSoftware/HomePage>).

Each image was corrected for RF inhomogeneity non-uniformity (Sled, Zijdenbos, & Evans, 1998) and the three T1 and T2-weighted images were averaged together following rigid-body alignment (Collins, Neelin, Peters, & Evans, 1994) in order to decrease noise and increase

contrast. Each image was then normalized to a fixed intensity range (0–10,000), and intensity-averaged on a voxel-by-voxel basis to enhance signal and contrast (Holmes et al., 1998) to produce one final T1, and T2-weighted image volume. T1- and T2-weighted averages were then rigidly aligned to one another (Collins et al., 1994) to allow for neuroanatomical homology between the contrasts.

## 2.2 Manual Tracing Protocol

Whereas past protocols have only involved manual tracings of the fornix, the present study seeks to delineate the left and right alveus, fimbria, and fornix using the high-resolution images described above. In addition, the protocol is tailored to fit with our previously published protocol for segmentation of the HF subfields (Winterburn et al., 2013). A variety of different anatomical papers and print atlases were used to create the WM atlases (e.g. Duvernoy et al., 2013; Mai, Majtanik, & Paxinos, 2015; Talairach & Tournoux, 1988) and segmentations were additionally inspected for anatomical accuracy by author JCP. All tracings were completed using the Display software package (part of the MINC toolkit:

<http://www.bic.mni.mcgill.ca/ServicesSoftware/HomePage>). In general, contrast differences were used to discern the WM from the HF grey matter and surrounding structures. In areas of anatomical uncertainty, geometrical rules were applied to maintain a consistent approach that approximates the known neuroanatomy while allowing the protocol to be effectively replicated by others; a strategy successfully employed by our group (Park et al., 2014; Winterburn et al., 2013) and others (Ekstrom et al., 2009; Kerchner et al., 2010; La Joie et al., 2010; Libby, Ekstrom, Ragland, & Ranganath, 2012; Malykhin, Lebel, Coupland, Wilman, & Carter, 2010; Mueller & Weiner, 2009; Palombo et al., 2013; Pluta, Yushkevich, Das, & Wolk, 2012; Preston et al., 2010; Pruessner et al., 2000; Wisse et al., 2012; Yushkevich et al., 2009; 2010). Similarly, this has also been the case for the application of histologically derived MR atlases (Adler et al., 2014) where visual inspection of such atlases has also been used in conjunction with other atlases to

approximate borders of HF subfields in head and tail sections (Yushkevich, Pluta, et al., 2015b). Although T1-weighted scans were mainly used to guide segmentation, T2-weighted scans proved useful as a second anatomical reference (most notably in areas where the T2 contrast provided more visibility; e.g. the anterior pillars of the fornix or WM posterior to the crux of the fornix). Given that the present WM structures have a complex three-dimensional shape (e.g. fornix twists and turns in and out of various planes), all views were employed to aid delineation. Some of the WM structures may be more visible in one plane (i.e. sagittal, coronal, axial) than another. For similar reasons, 3D surface representations of segmentations were used to guide tracing in ambiguous areas and to enforce strict neuroanatomical homology. The description provided below represents only a summary of the devised tracing protocol. A comprehensive version of the protocol with specific written guidelines per structure and corresponding 17 anatomically detailed images, can be found in Supplementary Materials Section 1.2: Manual Tracing Protocol.

***General anatomy of the alveus, fimbria, and fornix:*** The human HF is a curved cylindrical-like brain structure located in the MTL. The HF exists bilaterally and consists of a coiled elaboration of the cerebral cortex extending medially in the anterior-posterior direction. The HF rises slightly dorsally along its long-axis when moving from anterior to posterior and is enveloped by WM protruding from within the HF. These myelinated fibers envelop the HF and, for the most part, contour its trajectory through the medial temporal lobe until they aggregate near the HF tail and curve superiorly and anteriorly, projecting to the mammillary bodies. The alveus covers the majority of the anterior and superior portion of the HF head. It also extends along the length of the HF, appearing along the wall of the lateral ventricle, located superolateral on the surface of the HF. Tracts comprising the anterior, lateral and posterior sections of the alveus move medially and give rise to a concentrated fiber bundle; the fimbria. The fimbria which appears along the superomedial edge of the HF is considerably larger, and thus, more visible than the alveus.

Moving posteriorly, the fimbria then transitions into the crux of the fornix. At this point the WM

tracts of the fornices move superiorly and anteriorly continuing through the midline of the brain. As the fornices travel through the center of the lateral ventricles, both fornices (left and right) merge to form the body of the fornix. Finally, anterior to this, both fornices separate and descend to form the anterior pillars of the fornix, and connect with the mammillary bodies (see Supplementary Materials Section 1.1: General Anatomy of Alveus, Fimbria and Fornix).

**Alveus:** Identification of the alveus begins in the coronal plane in the anterior to posterior direction (all other planes including 3D reconstruction were used to aid tracing). At its most anterior extremity, the alveus first appears as a circular/oval shape approximately 1mm prior to the emergence of the HF head as previously identified (Winterburn et al., 2013). At this point, all high-intensity WM voxels (similar to those of the corpus callosum or anterior commissure) are included as alveus; the superior border being the grey matter of the amygdala, and inferior border being the WM superior to the entorhinal and perirhinal cortices. Once the HF head emerges, the alveus sits atop the HF and is inferiorly bounded by the grey matter ribbon of the CA region (see Figure 1A, i). Since the WM of the alveus blends inferiorly with that of the WM superior to the parahippocampal gyrus, an approximation is made such that the alveus extends superiorly on the HF from the lateral-most extent of the HF to the medial most extent (see Figure 1A, ii, iii). In more posterior slices, the HF shifts superiorly towards the lateral ventricle. At this point the WM of the alveus extends more laterally and blends with the WM inferior to the HF. In order to ensure inclusion of voxels contained within the alveus, the lateral boundary is taken to be the point at which the WM of the alveus meets the floor of the lateral ventricle (Figure 1B, iv). Medially, the alveus is traced until it is no longer visible. While the inferior boundary remains the same as in previous slices, the superior boundary at this point now becomes the cerebrospinal fluid (CSF) of the lateral ventricle. For the most part, the alveus maintains the same boundaries from the HF body to the tail, running laterally and superiorly along the HF. Following the disappearance of the uncus of the HF head, the WM of the alveus and fimbria become

indistinguishable at the level of the HF body. Here, a geometric rule was devised to separate these two regions. This involved bisecting the entire WM ribbon superior to the HF with a vertical line down the middle of the top most undulation of the HF body (see Figure 1C, v). This measurement was taken to be the half-way point between the medial end of the CA4/DG (i.e. the medial-most termination of CA4/DG and the stratum radiatum, lacunosum and moleculare (SR/SL/SM) subregions as defined by Winterburn et al. (2013)) and the lateral most point of the HF WM, which extends out into the lateral ventricle. All WM occurring lateral to this vertical line was demarcated as alveus. In posterior sections near the HF tail, the high intensity signal contrast of the WM ribbon begins to decrease with each consecutive slice until it completely disappears. Segmentation of the alveus therefore terminated on the last slice on which it was discernible.

**Fimbria:** Moving along the HF from anterior to posterior in the coronal plane, segmentation of the fimbria begins once the uncus sulcus appears. In the case of the fimbria, all cardinal orthogonal planes were used to aid tracing. Similar to the alveus, the fimbria is superiorly bordered by the CSF and inferiorly bordered by the grey matter of the uncus of the HF head. At the level of the uncus, the fimbria extends laterally until it reaches the lateral most undulation of the HF. This point coincides with the medial termination of the CA2/3 and DG/CA4 regions in our previous HF subfield atlas (Winterburn et al., 2013). The fimbria continues medially until the high intensity WM ribbon is no longer visible. In more posterior coronal sections, the fimbria begins to separate from the uncus and is flanked by the alveus. At the level of the HF body, a vertical line is drawn bisecting the WM ribbon on top of the HF, exactly half-way up the lateral-most undulation of the HF (Figure 1C, v). All WM medial to this line is included as fimbria. All other border definitions remain the same. Tracing of the fimbria continues until the crux of the fornix is in full view coronally (Figure 1E, vi).

**Fornix:** Tracing of the fornix begins in the coronal plane once the crux of the fornix is in full view (Figure 1E, vi). All other planes including 3D surface representations were also used to aid tracing. At this point, the fornix is bound inferomedially by the pulvinar nucleus of the thalamus and by the CSF of the quadrigeminal cistern. Since the WM of the fornix blends superiorly with the WM of the corpus callosum (Figure 1E, vii) and the commissure of the fornix, a reliable geometric rule to maintain tracing accuracy was employed. This involved tracing the WM along the angle where the fornix meets the superior WM from its lateral to medial edge (Figure 1E, red line). The lateral boundary of the fornix at this point is the medial edge of the alveus. In more posterior sections the WM of the fornix becomes removed from the WM of the corpus callosum and is traced until it is no longer visible. Tracing in the coronal plane ensues anterior to the crux of the fornix where the fornix moves superiomedially and anteriorly. The fornix takes a flattened appearance as its inferior, medial, and lateral aspects are all bordered by the CSF of the lateral ventricle. Here, the superiomedial border is the same as listed previously (Figure 1I, red line). The fornix then detaches from the corpus callosum (Figure 1H, viii) and tracing includes only the condensed area of high-intensity WM. These demarcations continue throughout the body of the fornix coronally until the anterior pillars of the fornix are reached (Figure 1F). At this point, the fornix moves inferiorly in two separate columns to meet the mammillary bodies. At this point, the axial view of the T2-weighted images is best used to trace WM of the fornix.

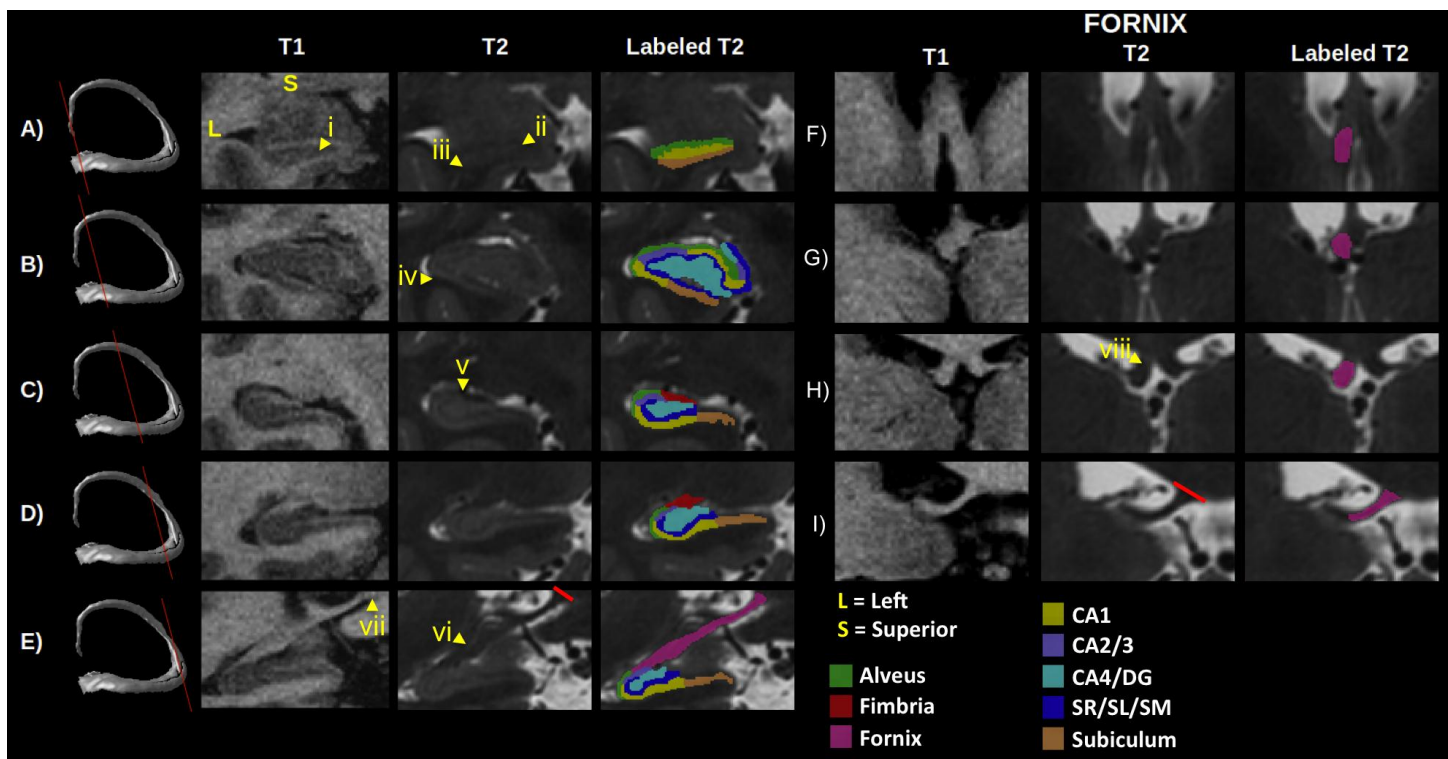


Figure 1. Example of segmentation protocol for the alveus, fimbria, and fornix. Columns A-E show unlabeled coronal slices for the white matter regions. Representative slices of the fornix are also included in rows F-I. White matter labels are presented along side hippocampal subfield labels from Winterburn et al. (2013). Both T1 and T2 images were cross-referenced during tracing. Sagittal and axial sections were also used to guide tracing. A) Depicts tracing protocol for the alveus at the level of the anterior HF head region. The alveus is bordered superiorly by the grey matter of the amygdala and inferiorly by the grey matter of the hippocampus (i). Sitting on top of the hippocampus, it includes the white matter ribbon extending from the most medial extension of the hippocampus (ii) to the most lateral extension of the hippocampus (iii). B) Shows segmentation protocol for the alveus in the head of the hippocampus. The alveus is bordered superiorly by the cerebrospinal fluid (CSF) of the lateral ventricle, and inferiorly by the hippocampus. It extends medially over the hippocampal undulations until it is no longer visible. Laterally the alveus is traced until it reaches the point where it meets the end of the lateral ventricle (iv). C) The alveus maintains the same border definitions except for its medial extent. Due to the presence of the fimbria, the alveus continues medially half-way up the top most undulation of the hippocampal body (v). The white matter ribbon medial to this extent is taken to be fimbria. D) Coronal slice through more posterior regions of the hippocampal body. E) The fimbria is traced until the presence of the crux of the fornix (vi), while the alveus remains. At this point the fornix is continued superiomedia until it meets the white matter of the corpus callosum (vii). F) Anterior pillars of the fornix. Axial sections were most useful in identifying the anterior pillars of the fornix as they descend inferiorly to reach the mammillary bodies. G) Coronal section through the body of the fornix. All high intensity white matter of the fornix is included in segmentation. H) Coronal section through the posterior body of the fornix. The fornix at this level is surrounded by CSF. I) A section through the posterior fornix just prior to the crux of the fornix. Superomedially the fornix follows the same rule as in vii.

### 2.3 Reliability of Manual Segmentation

The alveus, fimbria, and fornix of all 5 high-resolution scans were segmented using the protocol described above. Both intra and inter-rater reliability was assessed and consisted of retracing three randomly selected brains bilaterally. In order to reduce artificial increases in accuracy due to rater memory, all manual segmentations were completed 6-18 months after

completion of initial segmentations by two authors of this manuscript: one who developed the majority of the protocol (RSCA) and another who was taught the protocol *de novo* (VL) based on the description provided in this manuscript. Both tracers used not only the same tracing program (MINC Display) and style (i.e. mouse and keyboard), but also maintained the same screen size, resolution and image intensities across all tracings. Reliability for WM regions was measured using Dice's Kappa (Dice, 1945), which measures the degree of overlap between test and re-test labels (1 = full overlap, 0 = no overlap).

## 2.4 Investigation of the Memory Circuit in Healthy and Pathological Aging

### 2.4.1 Healthy Aging Dataset: OASIS

The OASIS cross sectional dataset was used to assess variation in WM (i.e. alveus, fimbria, and fornix) through the course of healthy aging (Marcus et al., 2007). A composite dataset, OASIS includes T1-weighted images from a total of 416 participants aged 18-96 scanned at 1.5T (3-5 scans per subject at 1x1x1.25mm, then rigidly registered, averaged, and resampled to 1mm isotropic voxel dimensions). Clinical Dementia Rating (CDR) scores were provided for each subject where 0 = no dementia, 0.5 = very mild dementia, 1 = mild dementia, 2 = moderate dementia (Morris, 1993). To ensure that individuals suspected of having Alzheimer's disease or any existing cognitive impairment were excluded, 100 individuals with CDR scores greater than 0 were removed. A total of 316 individuals were used in the final analysis (See Table 1 for demographic information; see Supplementary Materials Section 1.3: Population Demographics for age/sex distributions).

**Table 1.** Demographic Information

Structure	OASIS	ADNI		
		Controls	MCI	AD
<b>n*</b>	316	47	69	35
<b>Age (years)</b>				
Range	18-94	70-85	55-88	57-89
Mean (SD)	45.17 (23.88)	75.11 (3.90)	75.01 (8.18)	74.23 (7.93)
<b>Sex</b>				
Females, n (%)	197 (62.3%)	29 (61.7%)	25 (36.2%)	23 (65.7%)

\*n represents the number of subjects within the given dataset used. Some subjects were excluded due to CDR scores or segmentation failure.

#### 2.4.2 Pathological Aging Dataset: ADNI1 3T baseline

Pathological aging data used in this article were obtained from the Alzheimer's Disease Neuroimaging Initiative (ADNI) database ([adni.loni.usc.edu](http://adni.loni.usc.edu)). The ADNI was launched in 2003 as a public-private partnership, led by Principal Investigator Michael W. Weiner, MD. The primary goal of ADNI has been to test whether serial magnetic resonance imaging (MRI), positron emission tomography (PET), other biological markers, and clinical and neuropsychological assessment can be combined to measure the progression of mild cognitive impairment (MCI) and early Alzheimer's disease (AD). For up-to-date information, see [www.adni-info.org](http://www.adni-info.org). The ADNI1 3T baseline dataset was used to assess the role of WM in pathological aging. This provided a healthy control group, an MCI group of 69 and an AD group (see Table 1 for demographic information; see Supplementary Materials Section 1.3: Population Demographics for age/sex distributions). Similar to the OASIS scans, all T1-weighted images maintained a 1mm isotropic voxel resolution.

#### 2.4.3 Image Pre-Processing

In order to facilitate the downstream segmentation pipeline, OASIS images underwent pre-processing with N4 nonuniform intensity normalization (Tustison et al., 2010) followed by

neck cropping. Preprocessed ADNI1 3T baseline data (i.e. gradwarp, B1 non-uniformity and N3 correction; Sled et al., 1998; Zheng, Chee, & Zagorodnov, 2009) were cropped to remove the neck. All images were quality controlled prior to, and following image processing for multiple MRI artifacts including motion artifacts (e.g. ringing, striping, or blurring), signal loss/susceptibility artifact, field of view clipping, and ghosting.

## 2.5 Automatic Segmentation: MAGeT-Brain Segmentation

Multiple automatically generated templates (MAGeT) Brain segmentation (Chakravarty et al., 2013; Pipitone et al., 2014) was used in conjunction with the 5 high-resolution atlases to derive automatically generated segmentations of the subfields and WM of the HF. MAGeT Brain employs multi-atlas label fusion via majority vote following a bootstrapping procedure that uses a template library composed of images from the dataset under analysis. In this manner, high-resolution atlases are used to segment this template set of individuals. The template library is then used to segment the entire dataset. Subjects in the template library may be purposely hand-picked in order to match the demographics of the larger cohort. This selection process is completed independently by hand prior to MAGeT Brain implementation. Aside from this, MAGeT Brain is a fully automatic segmentation pipeline and requires no human interaction. In the current study we implement MAGeT Brain with a total of 21 templates (both for OASIS and the ADNI datasets; as per Pipitone et al., 2014). Using nonlinear registration (Avants et al., 2008) each atlas was used to label each template library image. Each subject was then labeled using nonlinear registration between each image in the template library, yielding 105 (5 atlases x 21 templates) possible candidate segmentations for each subject. These candidate labels were then fused via majority vote to create the final label. With voxel-wise majority vote, each voxel is given the most frequent label at that specific voxel location amongst all 105 candidate segmentations. In this way, the label receiving the highest count in any given voxel becomes the final label. Images in the template library were chosen to represent the demographic spread

within each cohort under study. OASIS templates maintained a mean age of 42.70 (SD = 21.18 years and 52.38% female). For the ADNI cohort, templates chosen maintained a mean age of 74.23 (SD = 7.20, 52.38% female; 4 healthy controls, 12 MCI, and 5 AD). All 466 MAGeT-Brain outputs (315 OASIS, 151 ADNI) were assessed for quality via manual inspection on a slice-by-slice basis by one of the authors of the manuscript (RSCA). Quality control was based on specific set of rules where each segmentation was assigned either a score of 0 (fail), 0.5 (good pass), or 1 (excellent pass; see Supplementary Materials Section 1.4 for more information on our detailed quality control procedure). Proper implementation of the MAGeT Brain pipeline relies on supercomputing infrastructures. All computations were performed using the available supercomputer resources at the SciNet HPC Consortium (Loken et al., 2010). When run in such an environment, and in an embarrassingly parallel fashion, computation time typically requires 2-4 hours and may vary based on the type of input data.

## 2.6 Reliability of automatic segmentation

Although MAGeT-Brain has been previously validated for HF segmentation (Pipitone et al., 2014), an additional validation effort was made in order to verify if the WM regions defined above could be identified on standard 1mm isotropic T1-weighted acquisitions. In order to test the reliability of the MAGeT-Brain labels, MAGeT labels were generated from the OASIS reliability dataset (consisting of 30 individuals scanned twice with a delay of 1-89 days). A total of 20 individuals were used after exclusion for possible pathological conditions (see Section 2.4.1). Intraclass correlation coefficient (ICC) was used to assess the degree of correlation between the labels generated from the first and the second scan. Although this would provide a measure of precision, in order to test the accuracy of MAGeT brain segmentation, individual subject first scans were rigidly registered to the second scan (with 6 degrees of freedom; Avants, Epstein, Grossman, & Gee, 2008). Resulting transformations were used to transform the MAGeT labels calculated on the first scan of the subject into the space of the repeat scan. Dice's Kappa

was used to assess the degree of overlap between labels where 0 represents no overlap and 1 represents perfect overlap between labels:

$$\kappa = \frac{2a}{2a + b + c}$$

Here, the number of voxels in both segmentations is denoted by  $a$  while  $b + c$  represents the sum of voxels unique to each respective label. Although registration and resampling errors will confound the quality of this evaluation, we use this to establish a possible lower bound on MAGeT Brain segmentation reliability in the context of labeling standard T1-weighted MRIs.

An additional test for precision was completed which involved the use of a modified leave-one-out-cross validation (LOOCV), similar to the simulation approach presented in our previous work (Pipitone et al., 2014). In this approach, each high-resolution T1-weighted atlas is downsampled to 1 mm isotropic voxel dimensions, and automatically segmented using the remaining atlases. Similarly, the downsampled versions of the homologous manually derived labels are used as a gold standard for segmentation against automated evaluation. Each LOOCV round involved the selection of a single downsampled atlas image treated as a subject image to be segmented by MAGeT-Brain. Given that the final step of the MAGeT-Brain pipeline involves a majority vote and that an odd number of input atlases improves segmentation (Pipitone et al., 2014), all combinations of three input atlases were used. Thus, each downsampled atlas is segmented once using each possible combination of 3 of the 4 high-resolution atlases. Therefore, for each of the five atlases, a total of 4 segmentations were evaluated per run, resulting in combined total of  $5 \times 4 = 20$  segmentations evaluated overall. The template library was composed of all 5 downsampled atlases as well as 14 OASIS scans. Dice's Kappa was calculated for each of the 20 segmentations per region (via comparison to the downsampled gold standard labels).

## 2.7 Whole-Brain Volume Estimation

The OASIS and ADNI datasets include estimates of total intracranial volume (eTIV; as derived from FreeSurfer) and were used in subsequent analyses. Recently, an arguably more robust measure of total brain volume, brain extraction based on a nonlocal segmentation technique (BEaST; Eskildsen et al., 2012), has also been used in recent literature for providing whole-brain measures. Although results presented in the present paper include those using the eTIV as provided with each dataset, results were additionally run using BEaST outputs as a complementary measure (See Supplementary Materials Sections 2.2 and 2.3 for more information on BEaST).

## 2.8 Statistical Analysis

A general linear model (GLM) accounting for sex and eTIV was used to assess the relationship between volumes of the structures and age in the OASIS dataset. Models assessing age by sex interactions as well as the presence of quadratic and cubic effects of age were also assessed. Analysis was performed for the entire HF (i.e. combined subfields) and WM circuit (i.e. combined WM regions) first as a whole, then repeated for individual HF subfields and WM structures. Effect sizes (standardized  $\beta$  values) were calculated for each region. Multiple comparisons between all 16 subregions of the memory circuit were corrected for using Bonferroni correction (here, corrected threshold corresponds to  $p < 0.0031$ ; uncorrected  $p$  values are also reported). Pair-wise structural correlations were also assessed to test for volumetric relationships between all WM or HF subregions to determine if there were any significant subregion grouping patterns in the normative neurodegenerative process or if pairs of subfields and HF WM regions degenerated with a consistent patterning. Prior to correlation analyses, volumes were first residualized for effects of age, sex and eTIV. A correlation matrix was generated with a bootstrap of 10,000 iterations for matrices of the left and right volumes separately, and 100,000 times for the bilateral correlation matrix.

In the ADNI data, a GLM accounting for age, sex and eTIV, was used to assess differences in volume across controls, MCI, and AD groups. Once again, correction for multiple comparisons yielded a Bonferroni corrected significance level of  $p < 0.0031$  and standardized  $\beta$  values were also obtained for each region.

### 3.0 RESULTS

#### 3.1 Protocol Reliability

Intra-rater reliability values evaluated through Dice's Kappa revealed high reliabilities for WM regions, ranging from 0.81-0.90 (see Table 2). In addition, the assessment of inter-rater reliability demonstrated that reproducibility of the manual tracing protocol was high with Dice's kappa ranging from 0.81-0.87 (Table 2). The above results were comparable to those frequently reported and accepted in HF subfield literature (de Flores et al., 2015; Mueller et al., 2010; Olsen et al., 2013; Palombo et al., 2013; Winterburn et al., 2013; Wisse et al., 2012). Three-dimensional rendering was also used to qualitatively assess morphometric contiguity and was found to be of sufficiently smooth contours (See Figure 2).

**Table 2.** Summary of Intra/Inter-rater Reliability

Structure	Left Dice Score		Right Dice Score	
	Intra (range)	Inter (range)	Intra (range)	Inter (range)
Alveus	0.88 (0.90-0.85)	0.87 (0.89-0.85)	0.86 (0.90-0.75)	0.85 (0.86-0.83)
Fimbria	0.90 (0.92-0.89)	0.85 (0.87-0.83)	0.81 (0.86-0.71)	0.81 (0.84-0.77)
Fornix	0.89 (0.90-0.87)	0.81 (0.82-0.80)	0.84 (0.88-0.76)	0.81 (0.81-0.80)
Total White Matter	0.90 (0.90-0.89)	0.81 (0.84-0.75)	0.84 (0.89-0.76)	0.80 (0.86-0.74)

Average intra and inter-rater reliability was calculated using Dice's volumetric Kappa. A score of 0 represents no overlap between test and retest labels, whereas a value of 1 represents a complete overlap.

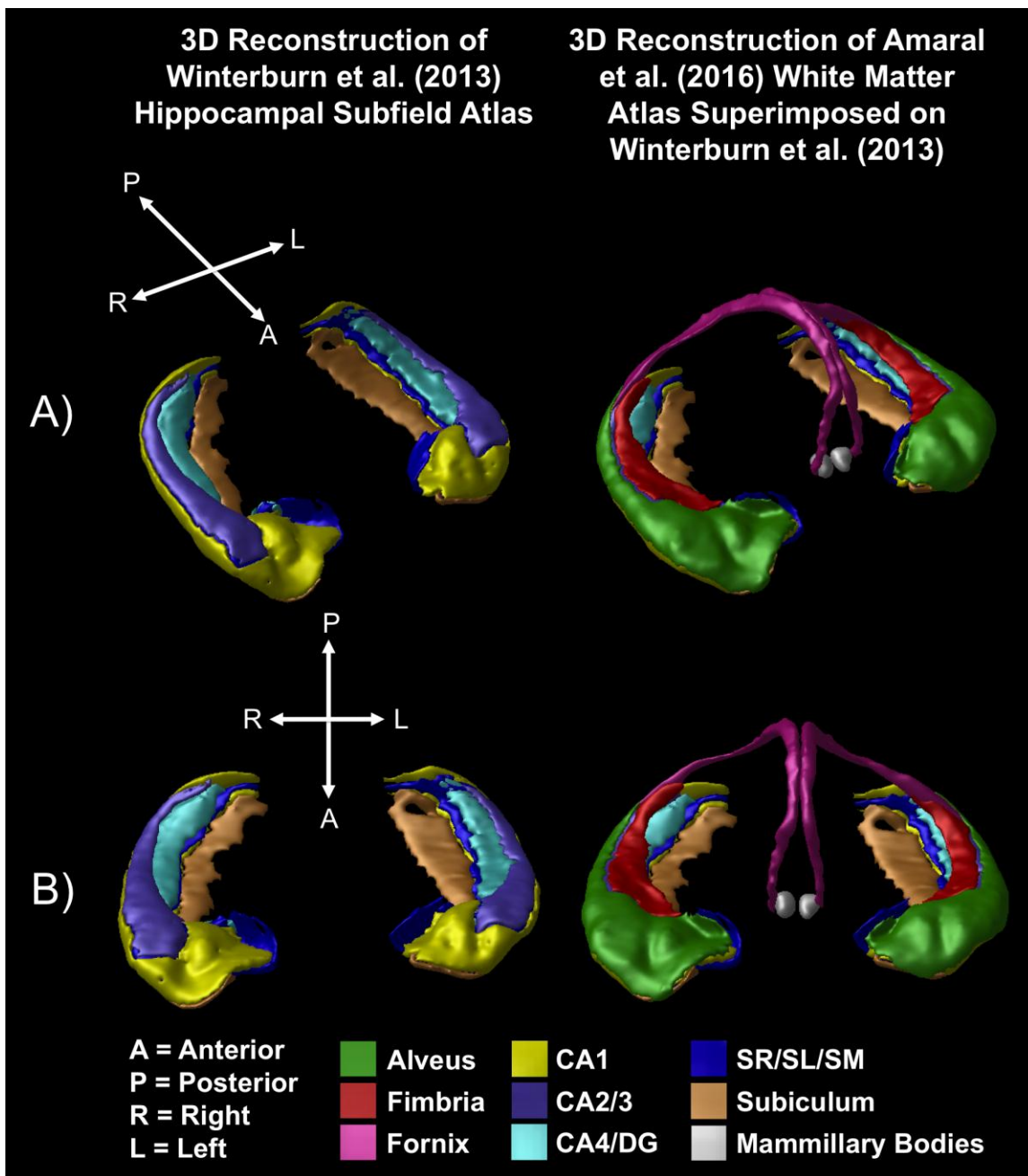


Figure 2. Three dimensional reconstruction of high-resolution hippocampal subfield and white matter atlases. Bilateral 3D reconstruction of the hippocampal subfields as per Winterburn et al. (2013) are depicted in the first column. The second column depicts the novel white matter labels superimposed on the Winterburn atlas. Row A) presents a lateral view of the bilateral hippocampi and white matter. Row B) presents a superior view of the hippocampal subfields and white matter.

### 3.2 Quality Control of MAGeT Brain Output

Segmentation quality control of the OASIS dataset resulted in 19 out of an initial 315 subjects (6.4%) being removed due to segmentation failure (see SM Table 1). ADNI quality control resulted in the exclusion of 6 individuals out of 151 (3.97%; see SM Table 1).

### 3.3 MAGeT Brain Reliability

Intraclass correlation coefficients (ICC) were used to assess the degree of correlation between the volumes generated from the first and the second OASIS scans. Results indicated a medium to high consistency for HF subfields and WM regions ranging from 0.79-0.99 (see Table 3; OASIS Validation). Dice's Kappa was used to assess the degree of overlap between labels and revealed values ranging from 0.61-0.84 (see Table 3; OASIS Validation). Results of the LOOCV analysis revealed Dice scores ranging from 0.30-0.70 for both HF subfields and WM structures. Although these validation results are comparable to previous work from our group for automatic HF subfields (Pipitone et al., 2014), results are lower than other groups (Van Leemput et al., 2009; Yushkevich et al., 2010; Yushkevich, Pluta, et al., 2015b). Despite this, it is important to note that validation efforts of the aforementioned groups have either 1) involved manual delineations of considerably fewer HF subfields, 2) HF subfields are only traced along the body of the HF and exclude all WM regions, and 3) automated segmentation is done on high-resolution MR images (as opposed to the 1mm isotropic standard resolution used in the present study).

**Table 3.** Summary of MAGEt Brain Validation

Structure	Left			Right		
	OASIS Validation		LOOCV	OASIS Validation		LOOCV
	ICC (SD)	Dice (SD)	Dice (SD)	ICC	Dice (SD)	Dice (SD)
CA1	0.95	0.77 (0.03)	0.57 (0.05)	0.98	0.76 (0.03)	0.50 (0.04)
CA2 & CA3	0.94	0.63 (0.06)	0.32 (0.09)	0.95	0.63 (0.08)	0.35 (0.10)
Dentate Gyrus/CA4	0.96	0.84 (0.02)	0.65 (0.04)	0.94	0.82 (0.03)	0.56 (0.05)
SR/SL/SM	0.96	0.68 (0.03)	0.39 (0.05)	0.96	0.65 (0.04)	0.30 (0.05)
Subiculum	0.96	0.73 (0.04)	0.52 (0.10)	0.96	0.75 (0.04)	0.41 (0.07)
Alveus	0.93	0.65 (0.05)	0.39 (0.07)	0.96	0.61 (0.05)	0.33 (0.06)
Fimbria	0.96	0.73 (0.05)	0.49 (0.09)	0.91	0.69 (0.08)	0.39 (0.11)
Fornix	0.99	0.80 (0.02)	0.70 (0.04)	0.99	0.79 (0.03)	0.67 (0.04)
White Matter	0.98	0.73 (0.04)	0.53 (0.7)	0.99	0.70 (0.05)	0.46 (0.06)
Hippocampus	0.98	0.73 (0.04)	0.49 (0.7)	0.99	0.72 (0.04)	0.42 (0.06)

Reliability values were assessed for each structure per hemisphere. MAGEt Brain labels of 20 OASIS subjects scanned at two different time points were used to assess the accuracy of MAGEt Brain segmentation. Reliability was conducted using Intraclass Correlation (ICC) which assesses the degree of volumetric correlation between test and re-test volumes. A score of 0 represents no correlation, a value of 1 represents a perfect correlation. In order to assess the precision of MAGEt Brain segmentation, labels produced from the first scan of each subject were rigidly aligned to their respective repeat scan. Kappa values were then calculated once labels were in the same space. Average reliability was assessed using Dice's volumetric Kappa which assesses the degree of overlap between test and re-test volumes. A score of 0 represents no overlap, a value of 1 represents a perfect overlap between test and re-test labels. An additional validation of MAGEt Brain employed the use of a leave-one-out-cross-validation (LOOCV) to assess segmentation precision. Reliability was assessed again using Dice's Kappa.

### 3.4 OASIS Dataset

No significant associations with age were found for combined WM volumes (i.e. sum of alveus, fimbria, and fornix; Left:  $R=0.03$ ,  $p=0.46$ ; Right:  $R=0.04$ ,  $p=0.82$ ). Out of all WM subregions, we observed a surprising positive association between bilateral alveus volumes and age (Left:  $R=0.35$ ,  $p<0.001$ ; Right:  $R=0.31$ ,  $p<0.001$ ; see Figure 3 A). Decreases in bilateral fornical volume through the adult lifespan were observed (Left:  $R=-0.15$ ,  $p=0.0012$ ; Right:  $R=-0.19$ ,  $p<0.001$ ; see Figure 3 C). The association between fimbria volume and age was less clear as the left fimbria volume decreased ( $R=-0.16$ ,  $p=0.0011$ ) and the right fimbria remained stable ( $R=-0.05$ ,  $p=0.91$ ; see Figure 3 B) in relation to age.

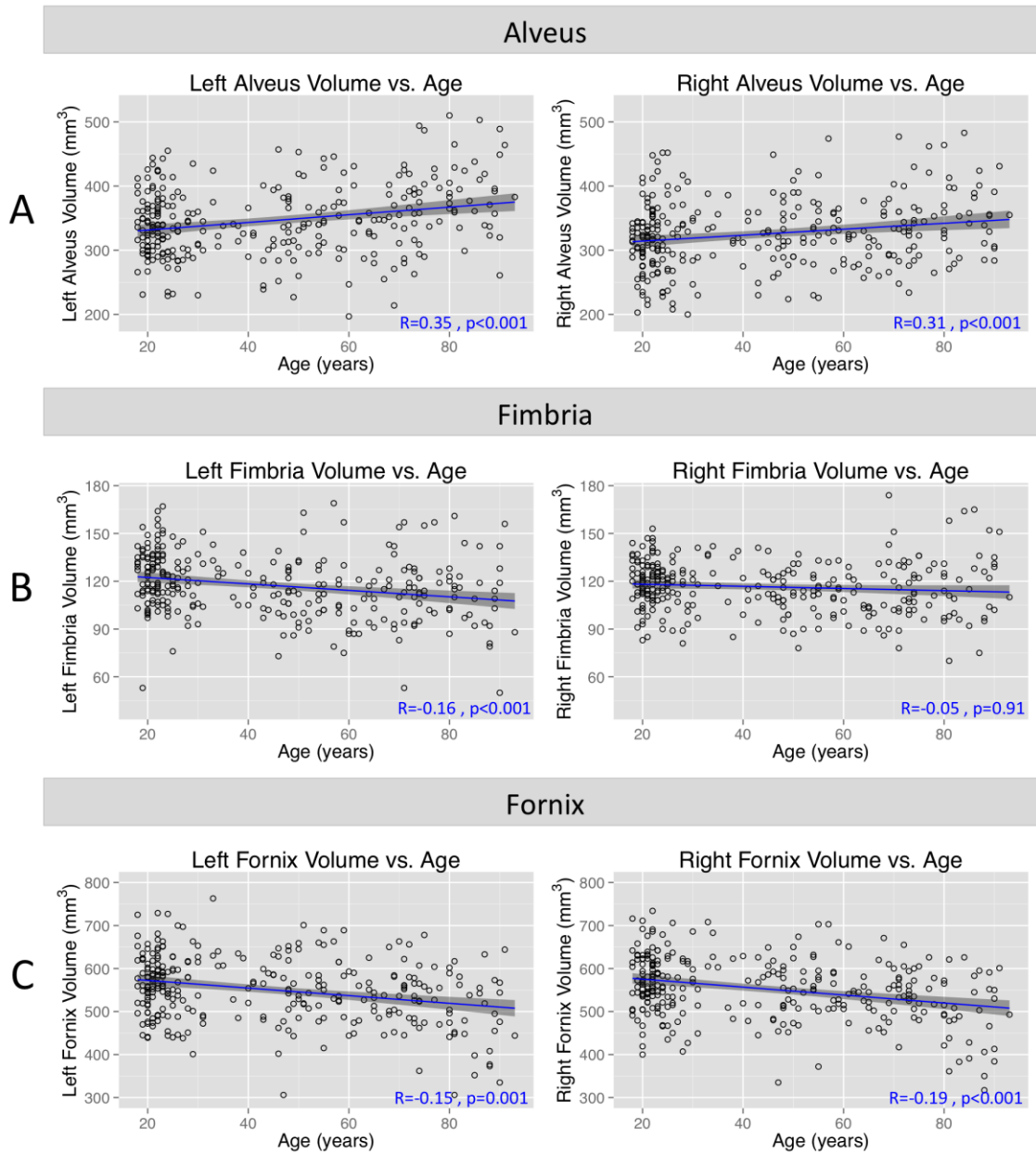


Figure 3. Scatter plots of white matter subfield volumes across age for 315 OASIS cases. Regression lines plotted depict volume as a function of age. Statistics reported are for a general linear model (GLM) accounting for sex and estimated total intracranial volume (eTIV). A: Plot of alveus volume as a function of age. GLM accounting for sex and eTIV demonstrated bilateral volume increases in the alveus (Left:  $R=0.35$ ,  $p<0.001$ ; Right:  $R=0.31$ ,  $p<0.001$ ). B: Plot of fimbria volume as a function of age. GLM accounting for sex and eTIV demonstrated a significant decrease for only the left fimbria ( $R=-0.16$ ,  $p<0.001$ ). The right fimbria was not significant ( $R=-0.05$ ,  $p=0.91$ ). C: Plot of fornix volume as a function of age. GLM revealed a bilateral decrease in fornix volume for both the left ( $R=-0.15$ ,  $p=0.001$ ) and right ( $R=-0.19$ ,  $p<0.001$ ) fornix. Plot depicts  $p$  and adjusted  $R$  values.

No significant relationship was observed for age with respect to whole HF volume (Left:  $R=0.04$ ,  $p=0.87$ ; Right:  $R=0.07$ ,  $p=0.077$ ) following Bonferroni correction. Significant associations

between age and some of the HF subfields were also observed. A positive association between age and volumes of left and right CA1 was found (respectively,  $R=0.66$ ,  $p<0.001$ ;  $R=0.21$ ,  $p<0.001$ ; Figure 4 A). The left CA4/DG demonstrated a trend toward volumetric decrease associated with age ( $R=-0.09$ ,  $p=0.035$ ) while the right did not show any such association ( $R=0.05$ ,  $p=0.937$ ; Figure 4 B). The left SR/SL/SM was found to decrease over time ( $R=-0.11$ ,  $p=0.014$ ; Figure 4 C), while the decrease in the right hemisphere did not reach significance ( $R=-0.01$ ,  $p=0.314$ ). No significant changes were found for the left and right subiculum (respectively,  $R=-0.03$ ,  $p=0.404$ ;  $R=0.05$ ,  $p=0.685$ ) or left and right CA2/3 regions (respectively,  $R=0.06$ ,  $p=0.867$ ;  $R=0.09$ ,  $p=0.054$ ). All linear models run using BEaST-derived total brain volumes did not deviate from findings reported above (see Supplementary Materials Section 2.2 for results). In addition, all substructures of the WM and HF were significantly associated with eTIV ( $p > 0.001$  for all) while also covarying for sex and age. Increased left CA4/DG and fornix volumes were observed for males compared to females ( $p = 0.03$  and  $p = 0.05$  respectively; covariates included age and eTIV) but did not survive Bonferroni correction.

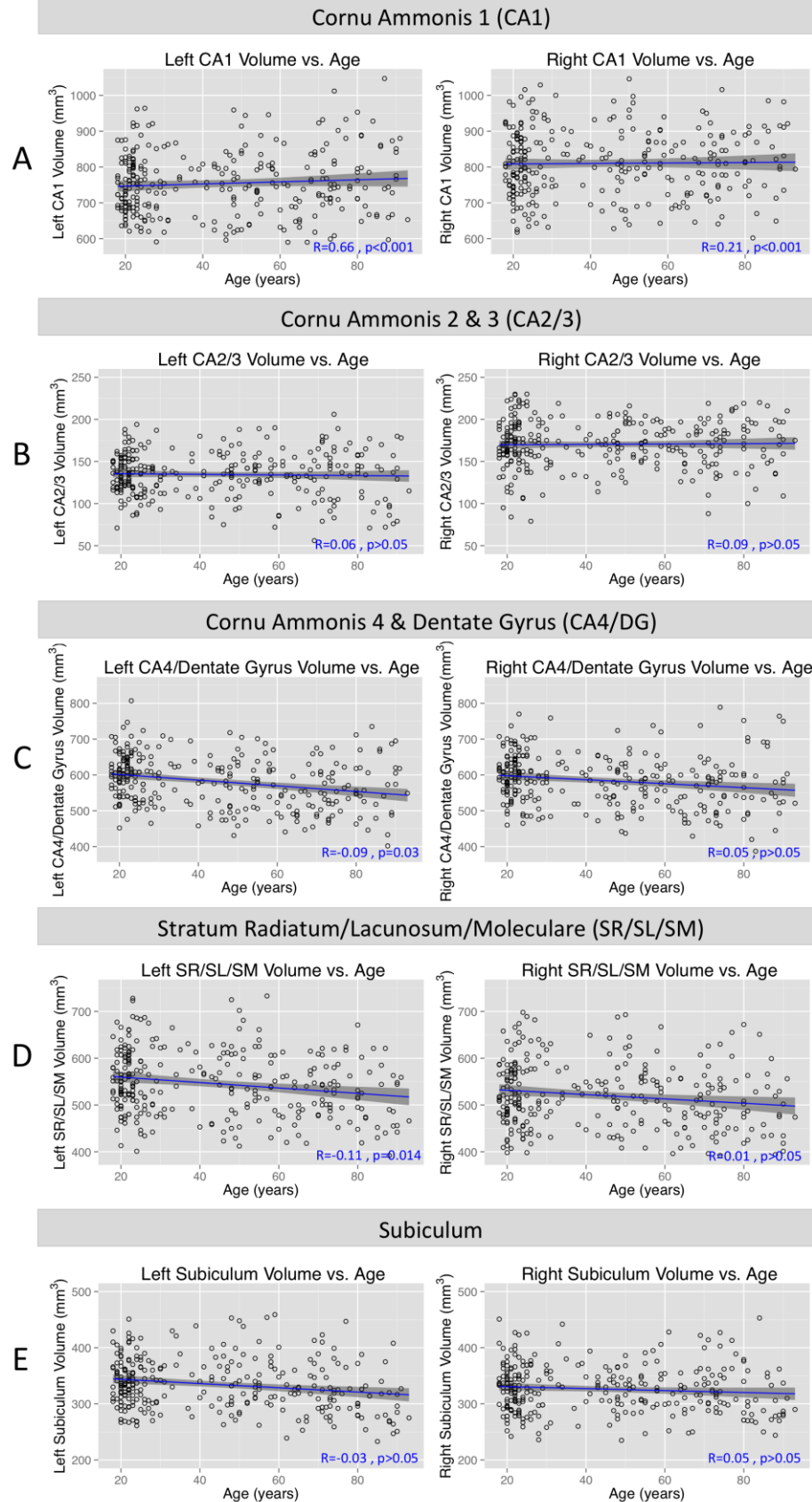


Figure 4. Scatter plots of hippocampal subfield volumes across age for 315 OASIS cases. Regression lines plotted depict volume as a function of age. Statistics reported are for a general linear model (GLM) accounting for sex and estimated total intracranial volume (eTIV). A: Plot of CA1 region volume as a function of age. GLM accounting for sex and eTIV demonstrated bilateral volume increases in the CA1 region (Left:  $R=0.66$ ,  $p<0.001$ ; Right:  $R=0.21$ ,  $p<0.001$ ). B: Plot of CA2/3 volume as a function of age. GLM revealed no significant changes for the left and right CA2/3 regions (respectively,  $R=0.06$ ,  $p=0.867$ ;  $R=0.09$ ,  $p=0.054$ ). C: Plot of CA4/DG volume as a function of age. GLM accounting for sex and eTIV demonstrated a significant decrease for only the left CA4/DG ( $R=-0.09$ ,  $p=0.035$ ). The right CA4/DG was not significant ( $R=0.05$ ,  $p=0.937$ ). D: Plot of SR/SL/SM volume as a function of age. GLM revealed a bilateral decrease in SR/SL/SM volume for the left ( $R=-0.11$ ,  $p=0.014$ ). The right SR/SL/SM showed no significant change ( $R=0.01$ ,  $p=0.314$ ). E) Plot of Subiculum volume as a function of age. GLM revealed no significant changes for the left and right subiculum (respectively,  $R=-0.03$ ,  $p=0.404$ ;  $R=0.05$ ,  $p=0.685$ ). Plot depicts  $p$  values and adjusted  $R$  values.

Bilateral increases of alveus volume over age maintained the largest effect size (left:  $\beta =0.84$ ; right:  $\beta =0.73$ ; see Figure 5). Largest negative effect sizes were observed for the left and right fornical volumes (respectively,  $\beta =-0.69$ ;  $\beta =-0.54$ ). Out of all white matter regions the left fimbria ( $\beta =-0.15$ ) showed the smallest effect size as it decreased in volume with age. Within the HF subfields, the bilateral CA1 region maintained the largest positive effect size (left:  $\beta =0.82$ ; right:  $\beta =0.94$ ) and largest negative effect sizes observed for the left CA4/DG ( $\beta =-0.32$ ) and left SR/SL/SM ( $\beta =-0.39$ ).

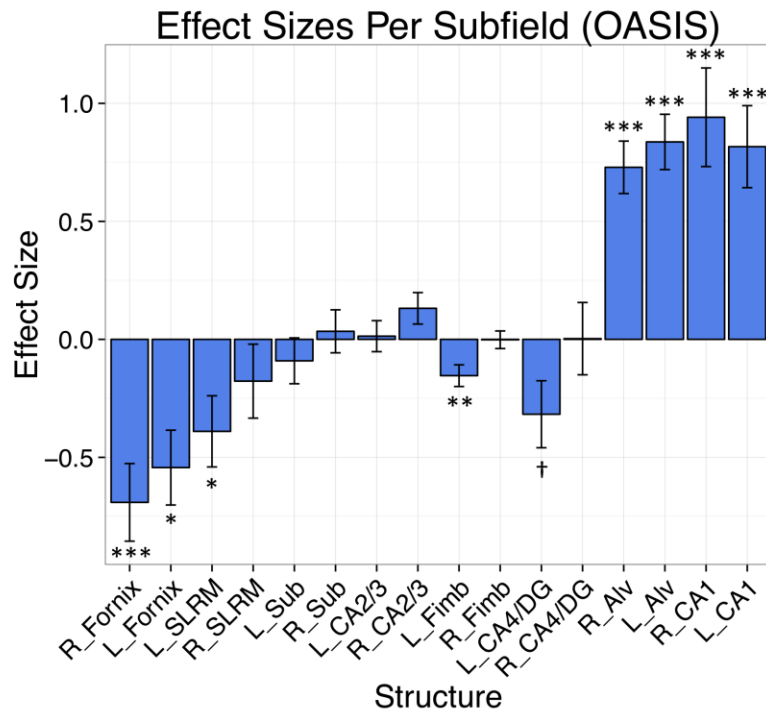


Figure 5. Graph depicting effect size ( $\beta$  values) of age on structure volumes. A general linear model accounting for sex, and total intracranial volume, demonstrated significant volumetric differences across age (post-Bonferroni correction) for the right and left fornix, right and left alveus, left fimbria, right and left CA1 region as well as the left SR/SL/SM. The left CA4/DG was found to be significant prior to Bonferroni correction. \* $p < .05$ , \*\* $p < 0.01$ , \*\*\* $p < 0.001$ , † indicates significance prior to Bonferroni correction.

A correlation matrix of the left and right volumes separately revealed generally positive correlations (Figure 6, A & B) with similar patterns across left and right hemispheres ( $p < 0.001$  for all  $r$ -values reported here). Namely the left CA1 region was significantly correlated to the left CA2/3 ( $r = 0.38$ ), CA4/DG ( $r = 0.64$ ) and SR/SL/SM ( $r = 0.74$ ) regions. This observed positive correlation was also observed for the right CA1 with CA2/3 ( $r = 0.58$ ), CA4/DG ( $r = 0.67$ ) and SR/SL/SM ( $r = 0.82$ ). In addition, the left alveus was positively correlated to the left CA1 ( $r = 0.54$ ), CA2/3 ( $r = 0.70$ ) and SR/SL/SM ( $r = 0.43$ ). Similar positive correlations were also observed for the right alveus with the right CA1 ( $r = 0.75$ ), CA2/3 ( $r = 0.70$ ) and SR/SL/SM ( $r = 0.65$ ). A bilateral correlation (Figure 6 C) revealed positive inter-hemispheric cross-correlations between the right alveus and left CA1 region ( $r = 0.59$ ) as well as the left alveus and right CA1 ( $r =$

= 0.52). Positive correlations were also observed between the right CA1 and left SR/SL/SM ( $r = 0.67$ ) as well as the left CA1 and right SR/SL/SM ( $r = 0.65$ ).

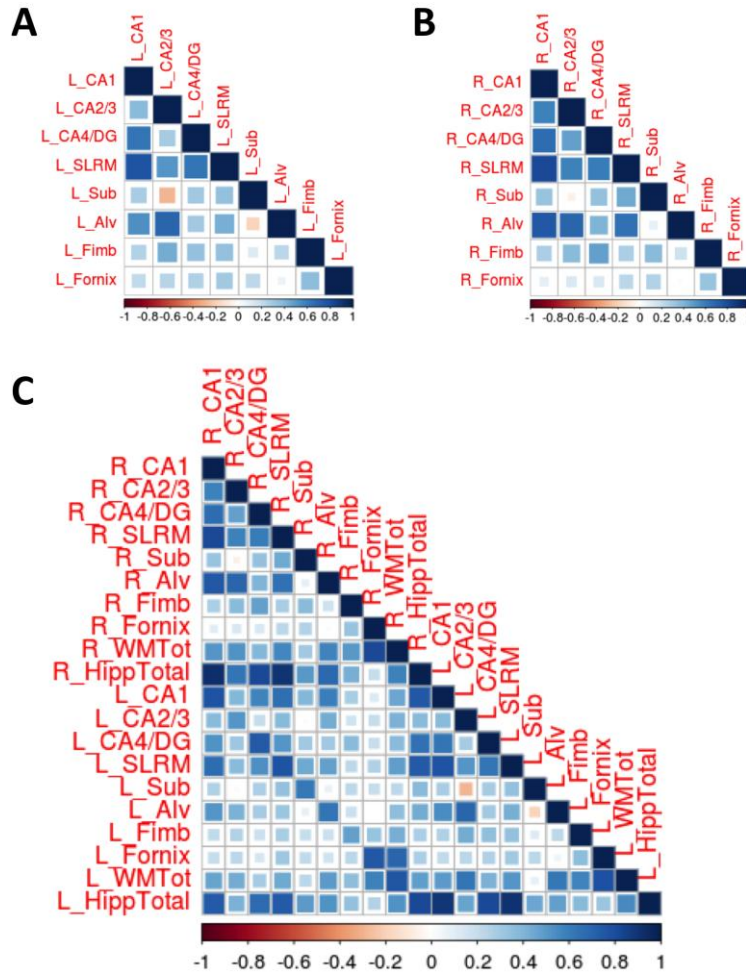


Figure 6. Structural correlation matrices of subfield volumes. A: Structural correlation matrix of left hemisphere subfields. Correlations were bootstrapped 1000 times. B: Structural correlation matrix of right hemisphere subfield volumes. Correlations were bootstrapped 1000 times. C: Structural correlation matrix of all subfield volumes bilaterally. Scale depicts degree of correlation (Pearson  $r$  value).

### 3.5 ADNI Dataset

In contrast to the OASIS results, a significant difference in combined WM volumes (i.e. alveus fimbria and fornix) were observed between the control and MCI group (Left:  $R = -0.19$ ,  $p = 0.0073$ ; Right:  $R = -0.18$ ,  $p = 0.016$ ; see Figure 7 B). A significant difference was also observed for HF whole volume between control and the MCI cohort (Left:  $R = -0.33$ ,  $p < 0.001$ ; Right:  $R = -0.24$ ,  $p < 0.001$ ; see Figure 7 A). Contrary to results observed in the healthy aging cohort, the

bilateral alveus did not show any significant differences between control and MCI groups (Left:  $R=0.24$ ,  $p=0.90$ ; Right:  $R=0.13$ ,  $p=0.33$ ; Figure 8 A). The left and right fimbria were found to decrease bilaterally (Left:  $R=-0.33$ ,  $p<0.001$ ; Right:  $R=-0.26$ ,  $p=0.003$ ; Figure 8. B), as did the fornix (Left:  $R=-0.23$ ,  $p=0.0043$ ; Right:  $R=-0.30$ ,  $p<0.001$ ; Figure 8 C) when comparing controls to MCI.

Between the MCI and AD cohorts no significant effect of diagnosis was found for all WM regions combined (see Figure 7 A). Trend-level differences were observed with respect to whole-HF volume differences (Left:  $R=-0.11$ ,  $p=0.079$ ; Right:  $R=-0.09$ ,  $p=0.13$ ; see Figure 7 B). Volumes of all WM subregions were not significantly different between MCI and AD except for the left fimbria, which was found to be significantly decreased in AD compared to MCI ( $R=-0.20$ ,  $p=0.029$ ).

Comparison between the control and AD groups yielded results that were strikingly similar to the control and MCI comparisons. AD demonstrated overall smaller combined WM volumes (Left:  $R=-0.30$ ,  $p<0.001$ ; Right:  $R^2=-0.20$ ,  $p=0.018$ ; see Figure 7 A), as well as the combined HF volume (Left:  $R=-0.52$ ,  $p<0.001$ ; Right:  $R=-0.42$ ,  $p<0.001$ ; see Figure 7 B). Unlike results for the normative aging sample, significant differences in alveus volume were not observed when comparing controls to the AD group. However, bilateral volume decreases were observed for both the fimbria (Left:  $R=-0.62$ ,  $p<0.001$ ; Right:  $R=-0.47$ ,  $p=0.001$ ), and fornix (Left:  $R=-0.26$ ,  $p=0.0063$ ; Right:  $R=-0.31$ ,  $p<0.001$ ). All above linear models were re-run using BEaST volumes as in the OASIS dataset and showed similar results (see Supplementary Materials Section 2.3 for results).

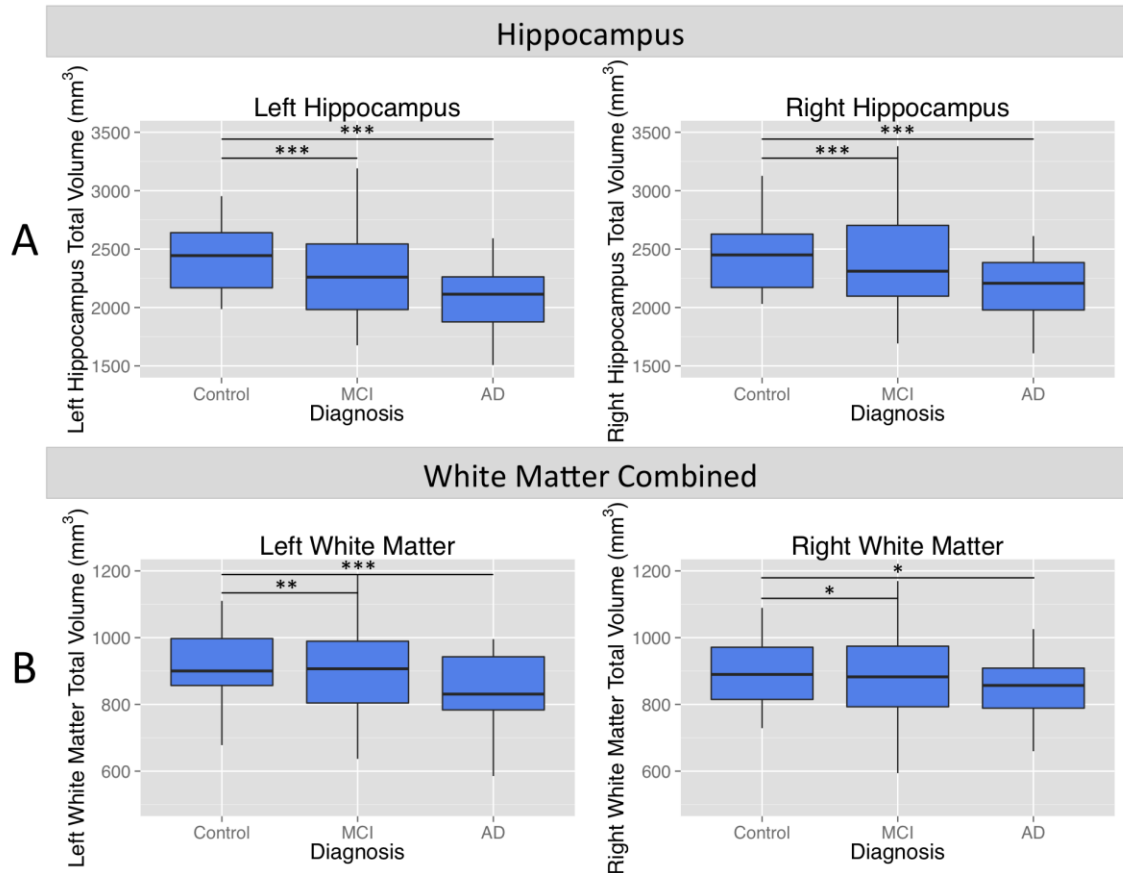


Figure 7. Boxplots of combined hippocampal subfield and white matter volumes for ADNI sample. A: Boxplot of whole hippocampal volume. Whole hippocampal measurement was obtained via the addition of all hippocampal subfield volumes (CA1, CA2/3, CA4/DG, Subiculum and SR/SL/SM). General linear model (GLM) accounting for age, sex and estimated total intracranial volume (eTIV) demonstrated bilateral volume decreases in the hippocampus when comparing the control cohort to the MCI group (Left:  $R=-0.33$ ,  $p<0.001$ ; Right:  $R=-0.24$ ,  $p<0.001$ ), and the Control to AD cohort (Left:  $R=-0.52$ ,  $p<0.001$ ; Right:  $R=-0.42$ ,  $p<0.001$ ). B: Boxplot of combined white matter volume. Combined white matter volume was obtained by the addition of all white matter subfield volumes (alveus, fimbria, and fornix). A GLM accounting for age, sex and eTIV demonstrated a significant decrease in combined WM volume when comparing Controls to the MCI group (Left:  $R=-0.19$ ,  $p=0.0073$ ; Right:  $R=-0.18$ ,  $p=0.016$ ), and Control to the AD group (Left:  $R=-0.30$ ,  $p<0.001$ ; Right:  $R=-0.20$ ,  $p=0.018$ ). \* =  $p<0.05$ , \*\* =  $p<0.01$ , \*\*\* =  $p<0.001$ .

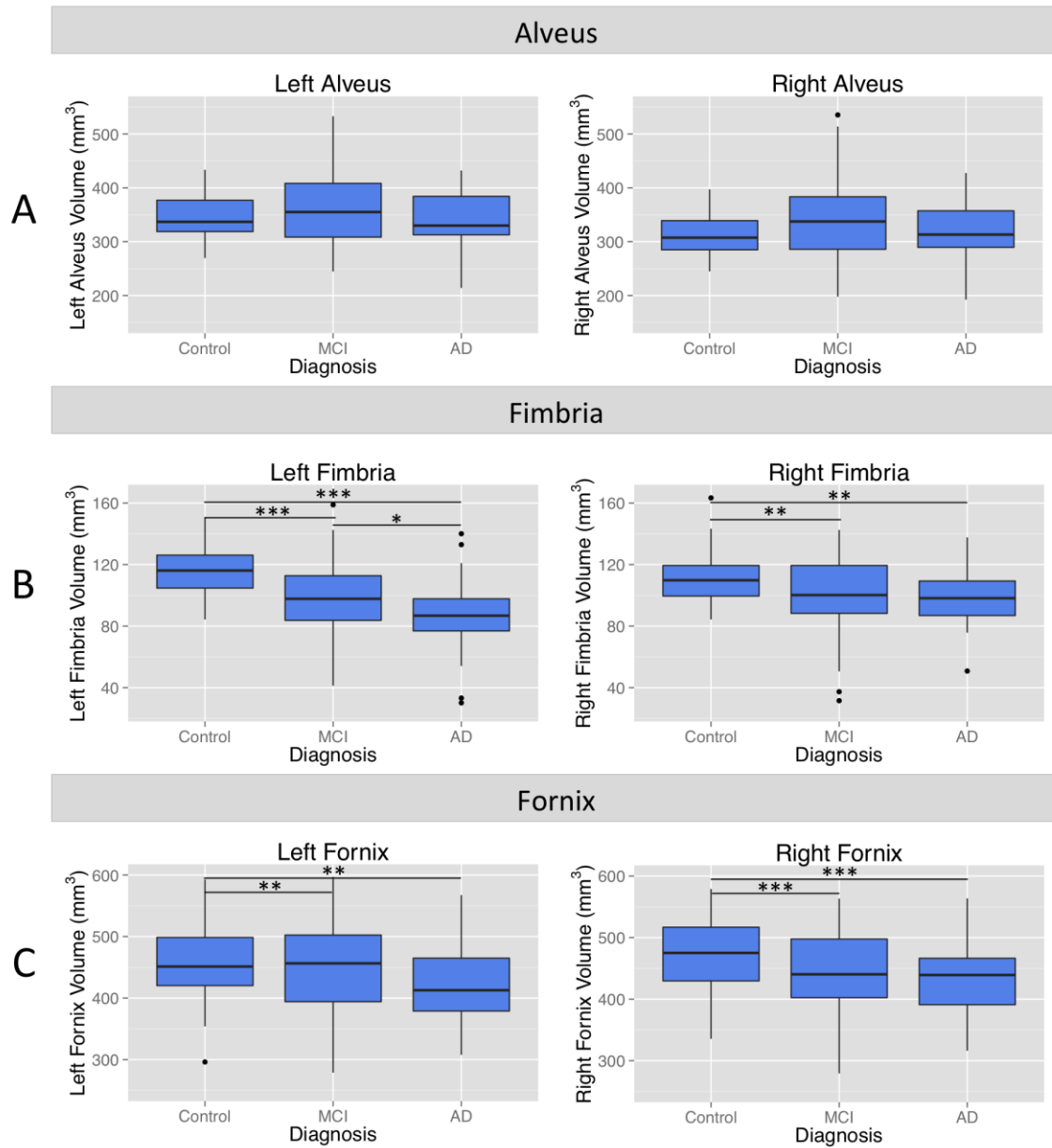


Figure 8. Boxplots of white matter subfield volumes for ADNI sample. A: Boxplots depicting left and right alveus volume by group. A general linear model (GLM) accounting for age, sex and estimated total intracranial volume (eTIV) demonstrated no significant differences comparing across all cohorts. B: Boxplots depicting left and right fimbria volume by group. A GLM accounting for age, sex and eTIV demonstrated a bilateral decrease in fimbria volume when comparing controls to the MCI cohort (Left:  $R=-0.33$ ,  $p<0.001$ ; Right:  $R=-0.26$ ,  $p=0.003$ ). The left fimbria was found to have a significant decrease ( $R=-0.20$ ,  $p=0.029$ ) when comparing volumes of the MCI cohort to those of the AD group. Finally volumes for the bilateral fimbria significantly decreased when comparing controls to the AD cohort (Left:  $R=-0.62$ ,  $p<0.001$ ; Right:  $R=-0.47$ ,  $p=0.001$ ). C: Boxplots depicting left and right fornix volume by group. A GLM accounting for age, sex and eTIV demonstrated a bilateral decrease in fornix volume when comparing controls to the MCI cohort (Left:  $R=-0.23$ ,  $p=0.004$ ; Right:  $R=-0.30$ ,  $p<0.001$ ). Comparing controls to the AD group, a significant decrease in the left and right fornix was also found (respectively,  $R=-0.26$ ,  $p=0.006$ ;  $R=-0.31$ ,  $p<0.001$ ). \* =  $p<0.05$ , \*\* =  $p<0.01$ , \*\*\* =  $p<0.001$ .

In direct contrast to the OASIS results, comparing controls to the MCI cohort (Figure 9 A), demonstrated significant decreases in left and right CA1 (respectively  $\beta = -61.1$  and  $\beta = -85.0$ ) and also more striking decreases in the left and right subiculum (respectively  $\beta = -43.2$  and  $\beta = -42.8$ ), left and right SR/SL/SM (respectively  $\beta = -67.7$  and  $\beta = -46.5$ ), left fimbria ( $\beta = -18.3$ ), and right fornix ( $\beta = -44.6$ ). The left and right CA4/DG regions (respectively  $\beta = -52.3$  and  $\beta = -43.2$ ) as well as the right fimbria ( $\beta = -12.7$ ) and left fornix ( $\beta = -34.2$ ) were significant prior to Bonferroni correction. When comparing controls to the AD cohort, significant effect sizes were observed for the left and right CA1 (respectively  $\beta = -114.0$  and  $\beta = -88.7$ ), left and right CA4/DG (respectively  $\beta = -74.3$  and  $\beta = -71.8$ ), left and right subiculum (respectively  $\beta = -67.9$  and  $\beta = -62.1$ ), left and right SR/SL/SM (respectively  $\beta = -87.3$  and  $\beta = -67.3$ ), left and right fimbria (respectively  $\beta = -29.9$  and  $\beta = -13.8$ ), and right fornix ( $\beta = -42.5$ ). The left fornix ( $\beta = -37.6$ ) was significant prior to Bonferroni correction. Lastly, the MCI versus AD group effect sizes (Figure 9 C) showed no significant effect sizes, although, the left and right subiculum (respectively  $\beta = -26.9$  and  $\beta = -21.7$ ), as well as the left fimbria ( $\beta = -11.8$ ) were significant prior to Bonferroni correction.

## Effect Sizes Per Subfield (ADNI)

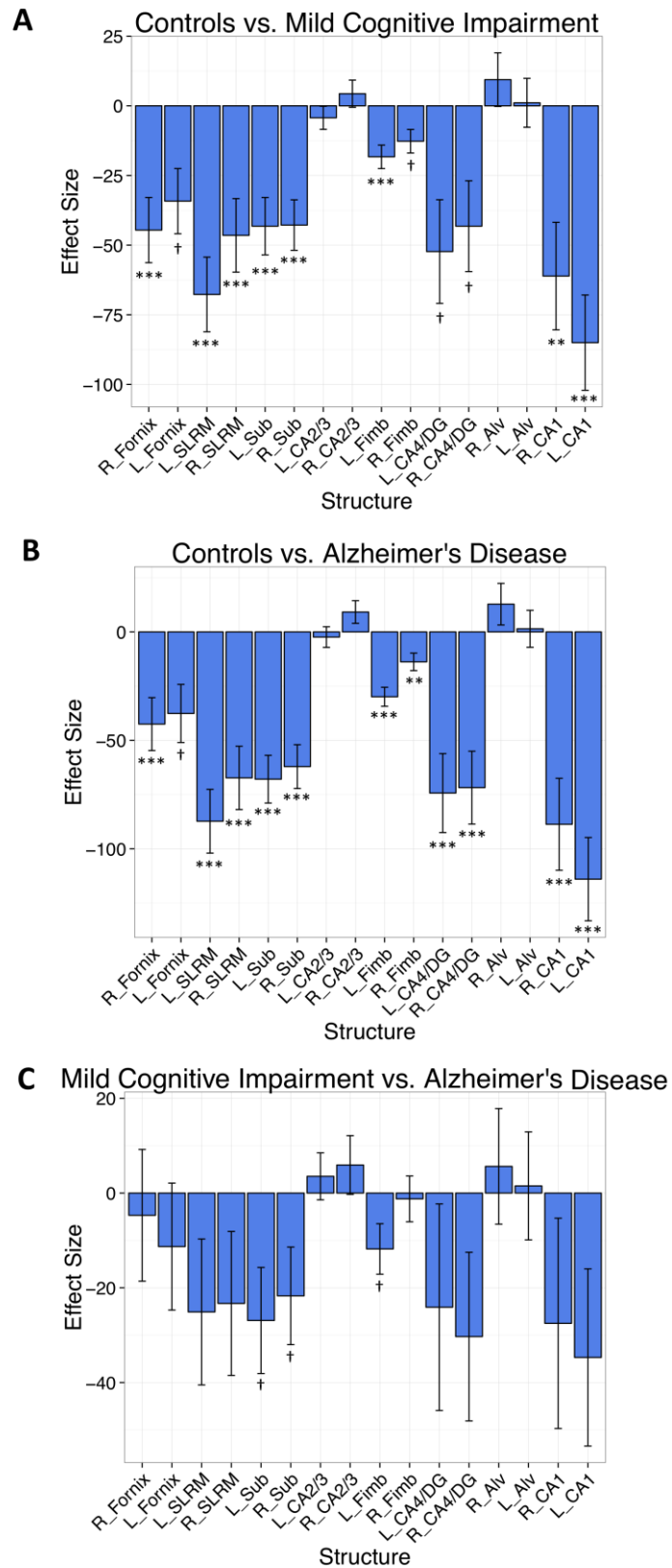


Figure 9. Graph depicting effect size ( $\beta$  values) of group status on structure volumes in ADNI sample. A general linear model (GLM) accounting for sex, and total intracranial volume was used to assess changes in volumes across all groups (post-Bonferroni correction). A: Effect sizes for controls versus MCI. Significant effect sizes were noted for the right and left CA1, right and left subiculum, right and left SR/SL/SM, left fimbria and right fornix. The left and right CA4/DG, right fimbria, and left fornix were also found to be significant prior to Bonferroni correction. B: Effect sizes for controls versus AD. Significant effect sizes were noted for the right and left CA1, right and left CA4/DG, right and left subiculum, right and left SR/SL/SM, right and left fimbria and the right fornix. The left fornix was found to be significant prior to Bonferroni correction. C: Effect sizes for MCI versus AD. No significant effect sizes were noted for all subregions. The right and left subiculum, and left fimbria were found to be significant prior to Bonferroni correction. \* $p < 0.05$ , \*\* $p < 0.01$ , \*\*\* $p < 0.001$ , † indicates significance prior to Bonferroni correction.

#### 4.0 DISCUSSION

In this paper we present a complete and comprehensive investigation of WM volumetry with respect to normal and pathological aging. This was accomplished via the creation, validation, and implementation of a novel methodological approach to the *in vivo* investigation of human extra-hippocampal WM. First, a detailed high-resolution segmentation protocol for the delineation of all WM outputs of the HF (i.e. alveus, fimbria and fornix) was developed and was found to be both reliable and reproducible; importantly we developed this protocol such that it is complementary to our existing work on the HF subfields (Winterburn et al., 2013). Secondly, we assessed the feasibility of using these manual segmentations as atlases for the automatic segmentation of HF subfields and WM by way of MAGeT-Brain segmentation. Our validation efforts demonstrated both appropriate precision and accuracy of MAGeT-Brain output segmentations at 1mm isotropic voxel dimensions. Finally, we assessed the volumetry of the WM structures in healthy and pathological aging by performing MAGeT-Brain segmentation on two different datasets, namely, the OASIS dataset (a healthy aging cohort) and the ADNI-1 3T baseline dataset (cohorts of controls, MCI and AD). While we hypothesized an overall decrease in WM and HF subregions over the course of healthy aging, we expected a stepwise decrease in

MCI to AD when compared to controls. Results indicated a preservation of the bilateral alveus and CA1 region over the course of healthy aging. Significant decreases were also noted for the bilateral fornix, left fimbria, and left SR/SL/SM regions. Comparison of the MCI cohort to controls indicated decreases in bilateral CA1, subiculum, SR/SL/SM, left fimbria and right fornix. While comparison of MCI to AD cohorts did not reveal any significant differences, the results observed for comparison of controls to AD remained markedly similar to those observed for MCI to controls with decreases observed in the bilateral CA1, CA4/DG, subiculum, SR/SL/SM, fimbria, and right fornix.

Manual segmentation has been a dominant approach for the study of HF subfields *in vivo*. Many protocols exist for the segmentation of the HF subfields (e.g. Bender, Daugherty, & Raz, 2013; Ekstrom et al., 2009; Kerchner et al., 2012; La Joie et al., 2010; Malykhin et al., 2010; Mueller et al., 2007; Olsen et al., 2013; Palombo et al., 2013; Winterburn et al., 2013; Wisse et al., 2012; Yushkevich, Pluta, et al., 2015b; Zeineh et al., 2012) including recent work towards the development of a unified protocol (Yushkevich, Amaral, et al., 2015a; see <http://www.hippocampalsubfields.com/>). However, little work has been done on the segmentation of the WM of the HF. Our work improves on previously published protocols for the segmentation of the fornix (see: Bilir et al., 1998; Copenhaver et al., 2006; Gale et al., 1995; Kuzniecky et al., 1999; Zahajszky et al., 2001). To the best of our knowledge, this work is the first to develop a detailed and reliable protocol for the full anterior to posterior segmentation of the alveus, fimbria, and fornix.

In addition to the above limitations observed in the segmentation protocols themselves, efficacy and quality of manual tracings also depend on field-strength, resolution, and scanning parameters used for acquisition. For example, many *in vivo* scanning protocols use highly anisotropic voxel

dimensions in the coronal plane with low-resolution through the anterior-posterior direction (2-3 mm; Kerchner et al., 2010; La Joie et al., 2010; Mueller et al., 2007; Mueller & Weiner, 2009; Olsen et al., 2013; Palombo et al., 2013; Van Leemput et al., 2009). While these types of acquisitions are advantageous since they reduce acquisition times, they introduce significant sampling bias in the measurement of small and geometrically complex structures and partial volume effects, possibly altering the visualization of clear boundaries. While our group has recently introduced methodological developments addressing the issues present in images with anisotropic voxels (Winterburn et al., 2013), an inherent trade-off with respect to scan-time remains. Although we do not explicitly quantify this trade-off (which would be difficult to complete in the absence of data from other groups) it is likely that systematic introduction of noise in images with anisotropic voxels can be more easily overcome with increases in sample size (relative to the isotropic acquisitions from our group). In addition, some groups who segment subfields at 7T (Kerchner et al., 2012; Kirwan, Jones, Miller, & Stark, 2007; Malykhin et al., 2010; Wisse et al., 2012; Zeineh et al., 2012) argue for more precise measures while most MR research is conducted using 3T scanners. Not only are the costs of 7T scanners high, but their absence in clinical settings may also hamper data availability and corresponding study investigation.

Given the advent of diffusion-weighted imaging (DWI), volume is not often considered a primary metric for the MR investigation of WM integrity. In contrast to the HF and MTL cortices, volumetric analysis of the WM structures in this circuit (i.e. the alveus, fimbria and fornix) have received significantly less attention. Instead, the majority of studies focus on DWI measures. Given the proximity to the lateral ventricles, standard DWI measures of these WM projections may suffer from partial volume effects, free water contamination, and inherent spatial, as well as angular resolution constraints, all of which limit its application to only the fornix (Pelletier et al., 2013; Zhuang et al., 2013). Although different pulse sequences (e.g. FLAIR) can be used to

eliminate the CSF partial volume effect, this often comes at a cost of lowering SNR, consequently downgrading fiber tracking results (Basser & Pajevic, 2000; Chou et al., 2005; D. K. Jones, 2003). In addition, standard DWI measures do not maintain the level of spatial detail needed to capture the alveus, fimbria, and areas of the anterior-most fornix. While tailored high-resolution DWI sequences can increase fiber tracking results, these protocols often take more time to employ, are highly specific, and subsequent analyses are generally more laborious to complete (Yassa et al., 2010; Zeineh et al., 2012). Therefore, volumetry of these regions may be a useful proxy of WM integrity and, potentially, a complementary analysis metric.

Advancements with respect to the automatic segmentation of HF subfields have been made over recent years (Fischl, 2012; Iglesias et al., 2015; Pipitone et al., 2014; Van Leemput et al., 2009; Yushkevich et al., 2010; Yushkevich, Pluta, et al., 2015b). Despite the use of high-resolution images as inputs by some algorithms (e.g. Yushkevich, Pluta, et al., 2015b), these images still suffer the same resolution constraints as mentioned previously. In addition, availability of such datasets are rare. On the other hand, the majority of automatic HF subfield segmentation has been completed on standard 1mm isotropic images (Fischl, 2012; Iglesias et al., 2015; Pipitone et al., 2014; Van Leemput et al., 2009; Voineskos et al., 2015). It can be argued that the dependability of using an automatic segmentation method on such data may result in imprecise measurements. Since the MAGeT-Brain algorithm uses a combination of whole HF anatomy and local contrast features (both of which are visible despite speculation in standard T1-weighted images), accurate and precise measurements should be possible. Our validation efforts were therefore motivated not only by this, but also due to the absence of any validation effort made on behalf of the aforementioned algorithms for segmentation of HF subfields on standard MR images (apart from our own in Pipitone et al., 2014). We demonstrated high accuracy as measured by ICC in our first of three validations. The high ICCs supported the reproducibility of MAGeT brain segmentation for all structures. Our corresponding two additional tests for

precision revealed lower but appropriate numbers. The Kappa values obtained following the transformation of OASIS labels into the same space represent a lower bound of reliability given the inherent error attributed with image registration. LOOCV results were similar to those previously reported by our group (Pipitone et al., 2014). Compared to other validation reports, our Dice's Kappa values were slightly lower than those reported in Yushkevich et al., (2009; Dice range of 0.51-0.74) and Yushkevich, Pluta, et al. (2015b; Control HF subfields Dice range of 0.50-0.82). However, it is important to differentiate between the two validations as they were obtained through validation directly on high-resolution images. As described in Pipitone et al. (2014), the resampling during the LOOCV combined with the use of only three atlases may have contributed to lower overlap scores (as we have previously demonstrated). The observed lower values for WM subregions were expected, yet are still impressive given that these structures are often 1-2 voxels thick and are spatially dynamic (i.e. twist, turn and move in and out of all planes). This especially holds true of the alveus, which maintained the lowest overall reliability. Further, the Dice metric penalizes structures with high surface area-to-volume ratios; precisely the type of geometry shown in the HF WM structures. Nonetheless, it is important to understand that structures with such low reliabilities may carry within themselves a bias when applied in an automatic segmentation framework. To our knowledge, this is the first attempt at validation, let alone automatic segmentation, of the HF subfields and alveus, fimbria and fornix on T1 1mm<sup>3</sup> standard MRI images. The use of 1mm isotropic data remains a limitation of the present study, with a trade-off made for image quantity over quality.

Compared to the study of AD and MCI, the investigation of HF subfields and WM with respect to healthy aging has been relatively limited. Consistent with our previous findings (Voineskos et al., 2015), no significant relationship with whole HF volume and age were observed, however the present study identified a strong preservation of the CA1. To date, few studies seem to support this result (La Joie et al., 2010; Voineskos et al., 2015). However, numerous studies have

demonstrated an opposite and linear decrease in CA1 volume throughout age (Mueller et al., 2007; Mueller & Weiner, 2009; Raz, Daugherty, Bender, Dahle, & Land, 2015; Shing et al., 2011; Wisse et al., 2014). It is important to note that these studies involve MR images at sub-millimeter voxel sizes, and consequently, lower participant numbers as compared to the present study. Nonetheless, other studies have used semi-automated methods (Kerchner et al., 2013) to show linear decreases in CA1 volume, while a recent automated investigation revealed no effect throughout age (Pereira et al., 2014). It has also been demonstrated that CA1 volume decline begins around the age of 50 in a nonlinear trajectory (de Flores et al., 2015). Some studies have also shown similar results to those presented in this manuscript regarding null changes in CA4/DG volume (de Flores et al., 2015; Kerchner et al., 2013; Mueller et al., 2007; Raz et al., 2015; Shing et al., 2011), yet a few studies support decreases with age (Mueller & Weiner, 2009; Pereira et al., 2014; Wisse et al., 2014; see de Flores et al., 2015, Table 3 for overview of studies investigating HF subfield structure in healthy aging). Heterogeneity in these results across laboratories may be a result of different methods used for segmentation, differing definitions of the subfields themselves, and/or differing use of covariates. For example, studies that use the Mueller protocol (Mueller et al., 2007) may suffer from a substantial bias, as this protocol only requires the demarcation of three coronal slices in the body of the HF. Further, other studies may or may not use brain volume as a covariate in their results.

No study to date has investigated changes in WM regions within the memory circuit. Thus, our results demonstrating preservation of the bilateral alveus and decreases in the left fimbria and fornices with age are the first to our knowledge. However, it should be stated that some WM regions, specifically the alveus, was an outlier in the analyses presented here. Regardless, while some volumetric studies investigating the fimbria have shown no change in volume across age (Frisoni et al., 2008; Pereira et al., 2014) the fornix has been extensively studied via DWI. Studies using quantitative fiber tracking corroborate our results by showing age-dependent reductions in

fornical structure (Schmahmann et al., 2007; Zahr, Rohlfsing, Pfefferbaum, & Sullivan, 2009), along with more recent DWI studies (Fletcher et al., 2013; Gunbey et al., 2014; C. Lebel et al., 2012; Sala et al., 2012; Sasson, Doniger, Pasternak, Tarrasch, & Assaf, 2013; Sullivan, Rohlfsing, & Pfefferbaum, 2010).

Research pertaining to the study of HF subfields within the context of AD and MCI has been reasonably more extensive. Previous high-resolution volumetric studies comparing the HF subfields in AD and control cohorts have replicated our observed findings of simultaneous decreases in subiculum, CA1, CA4/DG and SR/SL/SM volume together (Adachi et al., 2003; Boutet et al., 2014; de Flores et al., 2015; La Joie et al., 2010). Among all volumetric results in AD, observed decreases in the CA1 region occur most frequently and are often the central focus in such studies (Adachi et al., 2003; Boutet et al., 2014; de Flores et al., 2015; Iglesias et al., 2015; Kerchner et al., 2010; 2013; Khan et al., 2015; La Joie et al., 2013; Li, Dong, Xie, & Zhang, 2013; Lim et al., 2012; Mueller et al., 2010; Mueller & Weiner, 2009; Wisse et al., 2014; Yassa et al., 2010; Yushkevich, Pluta, et al., 2015b). Studies employing automatic segmentation completed at more standard resolutions akin to the present study have also been completed (Khan et al., 2015; Li et al., 2013; Lim et al., 2013) and have substantiated our results of decreases in the subiculum, CA2/3, CA2/DG and/or CA1. However, it is important to note that differences in segmentation protocols and atlases may partially explain the varying results among studies. While some fail to show volumetric changes in MCI cohorts (Kerchner et al., 2013; Wisse et al., 2014), a select few point towards focal decreases in CA1 (Mueller et al., 2010; Mueller & Weiner, 2009), CA3/DG, CA4/DG and/or the subicular subfields (de Flores et al., 2015; La Joie et al., 2013; Pluta et al., 2012). Some of the aforementioned automatic segmentation studies also included an MCI component, which resulted in similar results (Hanseeuw et al., 2011; Iglesias et al., 2015; Khan et al., 2015; Lim et al., 2012; Yushkevich, Pluta, et al., 2015b; see de Flores et al., 2015, Table 1 for overview of studies investigating HF subfield structure in MCI and AD).

With respect to WM regions, we found significant decreases in only the fornix and fimbria in both AD and MCI. Previous studies have demonstrated the accelerated atrophy of the fornix in AD volumetrically (Callen, Black, Gao, Caldwell, & Szalai, 2001; Copenhaver et al., 2006) along with a wide range of DWI studies (Jin, Shi, Zhan, & Thompson, 2015; Metzler-Baddeley, O'Sullivan, Bells, Pasternak, & Jones, 2012; Oishi, Mielke, Albert, Lyketsos, & Mori, 2012; Zhuang et al., 2013). While DWI work also implicates the fornix in MCI (Huang et al., 2012; Mielke et al., 2009; Oishi et al., 2012) the few existing volumetric studies have (Cui et al., 2012), and have not (Copenhaver et al., 2006) shown evidence of decreases in fornix volume. As for the fimbria, mixed evidence suggests both atrophy and preservation over MCI (Hanseeuw et al., 2011; Iglesias et al., 2015; Khan et al., 2015; Lim et al., 2013; Yushkevich, Pluta, et al., 2015b) and AD (Frisoni et al., 2008; 2006; Lim et al., 2013; Khan et al., 2015; Li et al., 2013). While no results were observed for the alveus, decreases in alvear volume have been both reported in AD (Boutet et al., 2014) and not found in MCI (Iglesias et al., 2015). Surprisingly, we did not observe significant differences for WM regions when comparing AD to MCI (that is, aside from the left fimbria). Although such differences have been reported (Mielke et al., 2009; Oishi et al., 2012) we found increasing negative effect sizes for the fornix and fimbria in aging to MCI and AD. Although not significantly step-wise, these results may support the conclusion that rates of atrophy in WM structures in healthy aging can serve as a predictor of conversion to MCI and AD (Fletcher et al., 2013).

Perhaps the most important goal of this study was to volumetrically assess the memory circuit in its entirety. In this way, each subfield could be evaluated within the context of all other structures, unlike most studies, which simply consider a few subfields irrespective of neighboring structures. This approach is necessary given the inherent connections present within the HF subfields and neighboring structures. In order to draw conclusions about atrophy and disease

changes, taking into consideration only sections of this circuitry is insufficient. By including the WM and the HF subfields we are able to reach this circuitry at a gross anatomical level. It is known that the HF has two main pathways: the polysynaptic pathway and the direct pathway (see Duvernoy et al., 2013 for review). Briefly, the polysynaptic pathway originates in the entorhinal cortex (Amaral & Insausti, 1990) and perforates the subiculum in order to synapse on the DG. From here, axons from the DG then synapse on those present in the CA4 and CA3. Axons then project to the CA1 followed by subiculum before leaving the HF via the alveus and fimbria. On the other hand, the direct pathway simply connects the entorhinal cortex to the CA1. Axons then synapse in the subiculum and back down to the entorhinal cortex (F. Du et al., 1993; MacLean, 1992). Taking into consideration that the entorhinal cortex is the first site of AD-related pathology (H. Braak & Braak, 1991; Gomez-Isla et al., 1996; Moreno et al., 2007; Whitwell et al., 2007) and that MR-identified structural atrophy has been shown to occur first in this region (Dickerson, 2001; A. T. Du et al., 2001; Killiany et al., 2000; 2002; Miller et al., 2015; Pennanen et al., 2004; Varon, Loewenstein, Potter, & Greig, 2011; Visser et al., 1999; see Zhou, Zhang, Zhao, Qian, & Dong, 2015 for review), our results are therefore justifiable at the circuit level. Specifically, early atrophy the entorhinal cortex may implicate the distal structures involved in its downstream circuitry. Since the first synapse of the direct pathway involves the CA1, the observed CA1 atrophy is logical. Our observed atrophy with respect to the subiculum and CA4/DG in AD/MCI can also be explained given the fact that these regions consecutively mimic the connections within the perforant pathway. Following this logic, atrophy beginning in one region would propagate to connecting regions occurring downstream. This idea fits with the cell-cell interaction hypothesis of AD (i.e. prion-like theory of AD) where the spread of pathogenesis is dependent on brain circuitry and spreads from cell to cell in a prion-like manner (Miller et al., 2015; Small, Schobel, Buxton, Witter, & Barnes, 2011; see Brundin, Melki, & Kopito, 2010, for general review; see Yin, Tan, Jiang, & Yu, 2014, for AD-relative review). In fact, these results have been mimicked in ex-vivo studies where the loss of afferents from the entorhinal cortex to

the DG can cause DG atrophy (Scheff, Price, Schmitt, & Mufson, 2006). Surprisingly, the final output afferents of the alveus were not found to suffer from volumetric changes despite that its deterioration has already been observed in AD (Mizutani & Kasahara, 1995).

Continuing with this line of thinking, the preservation of CA1 and alveus regions in our healthy aging sample can be explained by the possible strengthening of an older, more controversial pathway; the alvear pathway. Although its existence has been a subject of debate in humans, this pathway first described by (Cajal, 1911) has been shown in rats (Deller, Adelmann, Nitsch, & Frotscher, 1996). This is different than the perforant pathway since axonal projections here first travel through the alveus to reach the CA1 rather than perforating through the subiculum (Mizutani & Kasahara, 1995). Not only did we identify increases in alveus and CA1 volume throughout healthy aging, we also found structural correlations between these two regions. Taken together, these results could reveal some sort of neuroprotective effect mediated by the CA1 and/or alveus.

Despite the results obtained in the present study, perhaps the most salient limitation involved the use of cross-sectional and standard (1mm isotropic) MR images in our analyses. Although the use of such images provide inherently lower spatial information compared to high resolution images, the lack of dataset availability comprising of high resolution images for healthy aging, MCI and/or AD cohorts forced us to choose scan quantity over quality. While datasets like the Human Connectome Project (Van Essen et al., 2013) do exist and include 0.7mm isotropic scans of 897 healthy subjects aged 22-35, the limited age range forfeits the ability to complete a viable healthy aging study. This is also the case for retrospective or longitudinal data. However, despite this, it should also be understood that the population distributions used in the present study, specifically the ADNI cohorts, may too be a limiting factor. Ideally, the use of larger subject numbers balanced across cohorts would attest the results we have observed. Tied to such

resolution concerns is our use of subsampled versions of atlases during validation. Intuitively, downsampling atlases only provides a proxy gold standard label and may cause the loss of anatomical correctness due to resampling error. In addition, the devised WM protocol can only be thought of as an approximation of structure as rules and delineations are based on available print atlases and histological papers; a limitation suffered by most manual segmentation protocols that do not derive delineations from MRI data registered to histological data (e.g. Adler et al., 2014). In fact, the segmentation of structures with a unique anatomy and that also rely heavily on heuristic rules may carry a certain bias. For example, the natural shape of the alveus, along with its delineation used here may implicate its volumetric measure as a measure more akin to that of hippocampal shape, namely, length of the superolateral border of the HF. While the innate link between shape and volume cannot be exactly discerned here, the same case can be made for many other segmented subregions in their own right. In a similar fashion, volumetric measures of the CA1 may serve as a measure akin to the length of the HF inferolateral border. Despite this, volumetric segmentation, both manual and automatic, is largely based on contrast differences, those of which are properly captured in our automatic segmentations (See Supplementary Materials Figure 20). We hope that proper segmentation via contrast differences that change on a slice-per-slice basis and therefore determine a structure's thickness would identify such a measure as being a metric more akin to volume rather than shape. The unique anatomy of the alveus, fimbria, and fornix not only facilitates this differentiation, yet, also allows for the feasibility of registration of atlas labels to template-space of the MAGeT Brain algorithm. Unlike the majority of WM regions that appear uniform in conventional MRI, these regions are delimited by unambiguous boundaries, the majority of which include the CSF of the lateral ventricles and grey matter of the HF. Therefore, it would be feasible to suggest that sufficient boundary information is available and capable of driving registration, and ultimately proper volumetric-based segmentation.

It should be noted that other factors exist which may implicate the grey matter and WM contrast changes that provide the fundamental basis of our volumetric measures. Namely, age-related changes in grey matter/WM contrast differences have previously been reported (Salat et al., 2009) and have been shown to exhibit decreased contrast with increasing age (Vidal-Piñeiro et al., 2016). Consequently, it is reasonable to assume that tissue contrast may not be a constant property across age or neurodegenerative disorders. In fact, it has been shown that cortical thickness measures contingent on contrast differences also maintain a bias when contrast differences are not controlled for in healthy aging and AD cohorts (Westlye et al., 2009). Decreases in contrast have also been associated with whole-hippocampal volume measurements in AD cohorts (Salat et al., 2011). Similarly, motion has also been shown to affect multiple morphometric estimates of brain structure, reducing estimates of grey matter volume and thickness (Reuter et al., 2015). Motion artefacts have been shown to be age-dependent and increased amongst clinical groups, and have been shown to also affect volume albeit to a lesser extent than cortical thickness (Pardoe, Kucharsky Hieess, & Kuzniecky, 2016). While OASIS and ADNI provide their own quality control procedures, we instilled an additional quality control procedure in an effort to limit inclusion of scans with abnormal intensity inhomogeneity and motion. However, the contribution of such factors to our volumetric measures cannot be definitively excluded. Related to this is the concern that intensity characteristics of the 3T atlases used differ when compared to MR data acquired at lower field strengths (i.e. as in the OASIS 1.5T dataset). While the template step of the MAGeT Brain algorithm seeks to reduce registration errors, differences in data acquisition and image pre-processing techniques that implicate image intensity remain as a longstanding problem in automatic atlas-based segmentation. Furthermore, any error associated with atlas registration to images of different intensity information would be incorporated and evaluated in the validations performed herein. Such registration errors may be abated using a label fusion method that involves neighbourhood search. While our group has recently completed this for single label structures (Bhagwat et al.,

2016) this has yet to be completed for multiple labels and should be addressed in future work.

It is also important to highlight the need to compare our current methodology to that of other groups. Just as we have previously completed by our group for the whole HF (Pipitone et al., 2014; Bhagwat et al., 2016), comparison of our automatic white matter segmentation methods should be completed to that of others. However, given the lack of available comparative methods this is not yet possible. To date, the only comparative method that exists is FreeSurfer 6.0, which allows for the segmentation of the alveus and fimbria in addition to the hippocampal subfields. However, at this time, it is currently unavailable until further notice.

Here we have presented not only a novel protocol for the segmentation of WM structures, but have also validated its use for automatic segmentation via MAGeT Brain. Additionally, we assess the changes in these regions (along with HF subfields) in healthy aging and AD/MCI. We identified significant decreases in key WM and HF regions that follow the circuit-based patterns as theorized by the prion-like spread of AD pathology. Results support a neuroprotective role of the alveus and/or CA1 regions for healthy aging. Future study of WM regions and their relation to HF subfields are needed in both health and disease. The inclusion of MTL inputs (i.e. entorhinal, perirhinal or parahippocampal cortices) in future volumetric studies should be prioritized in order to achieve a more comprehensive assessment of the entire human memory circuit. This complete assessment would also offer insight into the circuit-based findings we observed. Finally, a comparison of DWI to volume metrics for the assessment of WM regions should be done in order to better understand which are most sensitive to observing changes in the alveus, fimbria and/or fornix.

## 5.0 ACKNOWLEDGMENTS

MMC is supported by the Fonds de Recherches Santé Québec, Canadian Institutes of Health

Research, National Sciences and Engineering Research Council of Canada, Weston Brain Institute, Alzheimer's Society, Brain Canada, and the Michael J. Fox Foundation for Parkinson's Research.

Computations were performed on the gpc supercomputer at the SciNet HPC Consortium (Loken et al., 2010). SciNet is funded by: the Canada Foundation for Innovation under the auspices of Compute Canada; the Government of Ontario; Ontario Research Fund — Research Excellence; and the University of Toronto.

Support for the acquisition of OASIS data was provided by the National Institutes of Health (P50 AG05681, P01 AG03991, R01 AG021910, P50 MH071616, U24 RR021382, R01 MH5684).

Data collection and sharing for this project was funded by the Alzheimer's Disease Neuroimaging Initiative (ADNI) (National Institutes of Health Grant U01 AG024904) and DOD ADNI (Department of Defense award number W81XWH-12-2-0012). ADNI is funded by the National Institute on Aging, the National Institute of Biomedical Imaging and Bioengineering, and through generous contributions from the following: AbbVie, Alzheimer's Association; Alzheimer's Drug Discovery Foundation; Araclon Biotech; BioClinica, Inc.; Biogen; Bristol-Myers Squibb Company; CereSpir, Inc.; Eisai Inc.; Elan Pharmaceuticals, Inc.; Eli Lilly and Company; EuroImmun; F. Hoffmann-La Roche Ltd and its affiliated company Genentech, Inc.; Fujirebio; GE Healthcare; IXICO Ltd.; Janssen Alzheimer Immunotherapy Research & Development, LLC.; Johnson & Johnson Pharmaceutical Research & Development LLC.; Lumosity; Lundbeck; Merck & Co., Inc.; Meso Scale Diagnostics, LLC.; NeuroRx Research; Neurotrack Technologies; Novartis Pharmaceuticals Corporation; Pfizer Inc.; Piramal Imaging; Servier; Takeda Pharmaceutical Company; and Transition Therapeutics. The Canadian Institutes of Health Research is providing funds to support ADNI clinical sites in Canada. Private sector contributions

are facilitated by the Foundation for the National Institutes of Health ([www.fnih.org](http://www.fnih.org)). The grantee organization is the Northern California Institute for Research and Education, and the study is coordinated by the Alzheimer's Disease Cooperative Study at the University of California, San Diego. ADNI data are disseminated by the Laboratory for Neuro Imaging at the University of Southern California.

## 6.0 REFERENCES

- Adachi, M., Kawakatsu, S., Hosoya, T., Otani, K., Honma, T., Shibata, A., & Sugai, Y. (2003). Morphology of the inner structure of the hippocampal formation in Alzheimer disease. *AJNR. American Journal of Neuroradiology*, *24*(8), 1575–1581.
- Adler, D. H., Pluta, J., Kadivar, S., Craige, C., Gee, J. C., Avants, B. B., & Yushkevich, P. A. (2014). Histology-derived volumetric annotation of the human hippocampal subfields in postmortem MRI. *NeuroImage*, *84*, 505–523. <http://doi.org/10.1016/j.neuroimage.2013.08.067>
- Amaral, D. G., & Insausti, R. (1990). The human hippocampal formation. In G. Paxinos (Ed.), *The Human Nervous System*. San Diego: Academic Press.
- Amaral, D. G., & Lavenex, P. (2007). Hippocampal neuroanatomy. In P. Andersen, R. Morris, D. G. Amaral, T. Bliss, & J. O'Keefe (Eds.), *The Hippocampus Book*. Oxford University Press.
- Andersen, P. (2007). *The Hippocampus Book*. Oxford University Press.
- Apostolova, L. G., & Thompson, P. M. (2008). Mapping progressive brain structural changes in early Alzheimer's disease and mild cognitive impairment. *Neuropsychologia*, *46*(6), 1597–1612. <http://doi.org/10.1016/j.neuropsychologia.2007.10.026>
- Avants, B. B., Epstein, C. L., Grossman, M., & Gee, J. C. (2008). Symmetric diffeomorphic image registration with cross-correlation: evaluating automated labeling of elderly and neurodegenerative brain. *Medical Image Analysis*, *12*(1), 26–41. <http://doi.org/10.1016/j.media.2007.06.004>
- Basser, P. J., & Pajevic, S. (2000). Statistical artifacts in diffusion tensor MRI (DT-MRI) caused by background noise. *Magnetic Resonance in Medicine*, *44*(1), 41–50. [http://doi.org/10.1002/1522-2594\(200007\)44:1<41::AID-MRM8>3.0.CO;2-O](http://doi.org/10.1002/1522-2594(200007)44:1<41::AID-MRM8>3.0.CO;2-O)
- Bender, A. R., Daugherty, A. M., & Raz, N. (2013). Vascular risk moderates associations between

- hippocampal subfield volumes and memory. *Journal of Cognitive Neuroscience*, 25(11), 1851–1862.  
[http://doi.org/10.1162/jocn\\_a\\_00435](http://doi.org/10.1162/jocn_a_00435)
- Bhagwat, N., Pipitone, J., Winterburn, J. L., Guo, T., Duerden, E. G., Voineskos, A. N., et al. (2016). Manual-Protocol Inspired Technique for Improving Automated MR Image Segmentation during Label Fusion. *Frontiers in Neuroscience*, 10, 325. <http://doi.org/10.3389/fnins.2016.00325>
- Bilir, E., Craven, W., Hugg, J., Gilliam, F., Martin, R., Faught, E., & Kuzniecky, R. (1998). Volumetric MRI of the limbic system: anatomic determinants. *Neuroradiology*, 40(3), 138–144.
- Boutet, C., Chupin, M., Lehericy, S., Marrakchi-Kacem, L., Epelbaum, S., Poupon, C., et al. (2014). Detection of volume loss in hippocampal layers in Alzheimer's disease using 7 T MRI: a feasibility study. *NeuroImage. Clinical*, 5, 341–348. <http://doi.org/10.1016/j.nicl.2014.07.011>
- Braak, H., & Braak, E. (1991). Demonstration of amyloid deposits and neurofibrillary changes in whole brain sections. *Brain Pathology (Zurich, Switzerland)*, 1(3), 213–216.
- Brundin, P., Melki, R., & Kopito, R. (2010). Prion-like transmission of protein aggregates in neurodegenerative diseases. *Nature Reviews. Molecular Cell Biology*, 11(4), 301–307.  
<http://doi.org/10.1038/nrm2873>
- Cajal, S. R. Y. (1911). *Histologie du système nerveux de l'homme & des vertébrés*.
- Callen, D. J., Black, S. E., Gao, F., Caldwell, C. B., & Szalai, J. P. (2001). Beyond the hippocampus: MRI volumetry confirms widespread limbic atrophy in AD. *Neurology*, 57(9), 1669–1674.
- Chakravarty, M. M., Steadman, P., van Eede, M. C., Calcott, R. D., Gu, V., Shaw, P., et al. (2013). Performing label-fusion-based segmentation using multiple automatically generated templates. *Human Brain Mapping*, 34(10), 2635–2654. <http://doi.org/10.1002/hbm.22092>
- Chételat, G., Fouquet, M., Kalpouzos, G., Denghien, I., la Sayette, De, V., Viader, F., et al. (2008). Three-dimensional surface mapping of hippocampal atrophy progression from MCI to AD and over normal aging as assessed using voxel-based morphometry. *Neuropsychologia*, 46(6), 1721–1731.  
<http://doi.org/10.1016/j.neuropsychologia.2007.11.037>
- Chou, M.-C., Lin, Y.-R., Huang, T.-Y., Wang, C.-Y., Chung, H.-W., Juan, C.-J., & Chen, C.-Y. (2005). FLAIR diffusion-tensor MR tractography: comparison of fiber tracking with conventional imaging. *AJNR. American Journal of Neuroradiology*, 26(3), 591–597.

- Collins, D. L., Neelin, P., Peters, T. M., & Evans, A. C. (1994). Automatic 3D intersubject registration of MR volumetric data in standardized Talairach space. *Journal of Computer Assisted Tomography*, *18*(2), 192–205.
- Copenhaver, B. R., Rabin, L. A., Saykin, A. J., Roth, R. M., Wishart, H. A., Flashman, L. A., et al. (2006). The fornix and mammillary bodies in older adults with Alzheimer's disease, mild cognitive impairment, and cognitive complaints: a volumetric MRI study. *Psychiatry Research*, *147*(2-3), 93–103. <http://doi.org/10.1016/j.psychresns.2006.01.015>
- Cui, Y., Sachdev, P. S., Lipnicki, D. M., Jin, J. S., Luo, S., Zhu, W., et al. (2012). Predicting the development of mild cognitive impairment: a new use of pattern recognition. *NeuroImage*, *60*(2), 894–901. <http://doi.org/10.1016/j.neuroimage.2012.01.084>
- de Flores, R., La Joie, R., Landeau, B., Perrotin, A., Mézence, F., La Sayette, de, V., et al. (2015). Effects of age and Alzheimer's disease on hippocampal subfields: comparison between manual and FreeSurfer volumetry. *Human Brain Mapping*, *36*(2), 463–474. <http://doi.org/10.1002/hbm.22640>
- Deller, T., Adelmann, G., Nitsch, R., & Frotscher, M. (1996). The alvear pathway of the rat hippocampus. *Cell and Tissue Research*, *286*(3), 293–303. <http://doi.org/10.1007/s004410050699>
- Dice, L. R. (1945). Measures of the Amount of Ecologic Association Between Species. *Ecology*, *26*(3), 297. <http://doi.org/10.2307/1932409>
- Dickerson, B. (2001). MRI-derived entorhinal and hippocampal atrophy in incipient and very mild Alzheimer's disease. *Neurobiology of Aging*, *22*(5), 747–754. [http://doi.org/10.1016/S0197-4580\(01\)00271-8](http://doi.org/10.1016/S0197-4580(01)00271-8)
- Du, A. T., Schuff, N., Amend, D., Laakso, M. P., Hsu, Y. Y., Jagust, W. J., et al. (2001). Magnetic resonance imaging of the entorhinal cortex and hippocampus in mild cognitive impairment and Alzheimer's disease. *Journal of Neurology, Neurosurgery, and Psychiatry*, *71*(4), 441–447. <http://doi.org/10.1136/jnnp.71.4.441>
- Du, F., Whetsell, W. O., Abou-Khalil, B., Blumenkopf, B., Lothman, E. W., & Schwarcz, R. (1993). Preferential neuronal loss in layer III of the entorhinal cortex in patients with temporal lobe epilepsy. *Epilepsy Research*, *16*(3), 223–233. [http://doi.org/10.1016/0920-1211\(93\)90083-J](http://doi.org/10.1016/0920-1211(93)90083-J)
- Duvernoy, H. M., Cattin, F., & Risold, P.-Y. (2013). *The Human Hippocampus*. Berlin, Heidelberg:

- Springer Science & Business Media. <http://doi.org/10.1007/978-3-642-33603-4>
- Eichenbaum, H., Yonelinas, A. P., & Ranganath, C. (2007). The medial temporal lobe and recognition memory. *Annual Review of Neuroscience*, *30*, 123–152.  
<http://doi.org/10.1146/annurev.neuro.30.051606.094328>
- Ekstrom, A. D., Bazih, A. J., Suthana, N. A., Al-Hakim, R., Ogura, K., Zeineh, M., et al. (2009). Advances in high-resolution imaging and computational unfolding of the human hippocampus. *NeuroImage*, *47*(1), 42–49. <http://doi.org/10.1016/j.neuroimage.2009.03.017>
- Eskildsen, S. F., Coupé, P., Fonov, V., Manjón, J. V., Leung, K. K., Guizard, N., et al. (2012). BEaST: brain extraction based on nonlocal segmentation technique. *NeuroImage*, *59*(3), 2362–2373.  
<http://doi.org/10.1016/j.neuroimage.2011.09.012>
- Fischl, B. (2012). FreeSurfer. *NeuroImage*, *62*(2), 774–781.  
<http://doi.org/10.1016/j.neuroimage.2012.01.021>
- Fletcher, E., Raman, M., Huebner, P., Liu, A., Mungas, D., Carmichael, O., & DeCarli, C. (2013). Loss of fornix white matter volume as a predictor of cognitive impairment in cognitively normal elderly individuals. *JAMA Neurology*, *70*(11), 1389–1395. <http://doi.org/10.1001/jamaneurol.2013.3263>
- Frisoni, G. B., Ganzola, R., Canu, E., Rüb, U., Pizzini, F. B., Alessandrini, F., et al. (2008). Mapping local hippocampal changes in Alzheimer's disease and normal ageing with MRI at 3 Tesla. *Brain : a Journal of Neurology*, *131*(Pt 12), 3266–3276. <http://doi.org/10.1093/brain/awn280>
- Frisoni, G. B., Sabattoli, F., Lee, A. D., Dutton, R. A., Toga, A. W., & Thompson, P. M. (2006). In vivo neuropathology of the hippocampal formation in AD: a radial mapping MR-based study. *NeuroImage*, *32*(1), 104–110. <http://doi.org/10.1016/j.neuroimage.2006.03.015>
- Gale, S. D., Johnson, S. C., Bigler, E. D., & Blatter, D. D. (1995). Nonspecific white matter degeneration following traumatic brain injury. *Journal of the International Neuropsychological Society : JINS*, *1*(1), 17–28.
- Gomez-Isla, T., Price, J. L., McKeel, D. W., Morris, J. C., Growdon, J. H., & Hyman, B. T. (1996). Profound loss of layer II entorhinal cortex neurons occurs in very mild Alzheimer's disease. *The Journal of Neuroscience : the Official Journal of the Society for Neuroscience*, *16*(14), 4491–4500.
- Gunbey, H. P., Ercan, K., Findikoglu, A. S., Bulut, H. T., Karaoglanoglu, M., & Arslan, H. (2014). The

limbic degradation of aging brain: a quantitative analysis with diffusion tensor imaging.

*TheScientificWorldJournal*, 2014(3), 196513–7. <http://doi.org/10.1155/2014/196513>

- Hanseeuw, B. J., Van Leemput, K., Kavec, M., Grandin, C., Seron, X., & Ivanoiu, A. (2011). Mild cognitive impairment: differential atrophy in the hippocampal subfields. *AJNR. American Journal of Neuroradiology*, 32(9), 1658–1661. <http://doi.org/10.3174/ajnr.A2589>
- Holmes, C. J., Hoge, R., Collins, L., Woods, R., Toga, A. W., & Evans, A. C. (1998). Enhancement of MR images using registration for signal averaging. *Journal of Computer Assisted Tomography*, 22(2), 324–333.
- Huang, H., Fan, X., Weiner, M., Martin-Cook, K., Xiao, G., Davis, J., et al. (2012). Distinctive disruption patterns of white matter tracts in Alzheimer's disease with full diffusion tensor characterization. *Neurobiology of Aging*, 33(9), 2029–2045. <http://doi.org/10.1016/j.neurobiolaging.2011.06.027>
- Iglesias, J. E., Augustinack, J. C., Nguyen, K., Player, C. M., Player, A., Wright, M., et al. (2015). A computational atlas of the hippocampal formation using ex vivo, ultra-high resolution MRI: Application to adaptive segmentation of in vivo MRI. *NeuroImage*, 115, 117–137. <http://doi.org/10.1016/j.neuroimage.2015.04.042>
- Jin, Y., Shi, Y., Zhan, L., & Thompson, P. M. (2015). Automated multi-atlas labeling of the fornix and its integrity in alzheimer's disease. *2015 IEEE 12th International Symposium on Biomedical Imaging (ISBI 2015)*, 140–143. <http://doi.org/10.1109/ISBI.2015.7163835>
- Jones, D. K. (2003). Determining and visualizing uncertainty in estimates of fiber orientation from diffusion tensor MRI. *Magnetic Resonance in Medicine*, 49(1), 7–12. <http://doi.org/10.1002/mrm.10331>
- Kerchner, G. A., Bernstein, J. D., Fenesy, M. C., Deutsch, G. K., Saranathan, M., Zeineh, M. M., & Rutt, B. K. (2013). Shared vulnerability of two synaptically-connected medial temporal lobe areas to age and cognitive decline: a seven tesla magnetic resonance imaging study. *The Journal of Neuroscience : the Official Journal of the Society for Neuroscience*, 33(42), 16666–16672. <http://doi.org/10.1523/JNEUROSCI.1915-13.2013>
- Kerchner, G. A., Deutsch, G. K., Zeineh, M., Dougherty, R. F., Saranathan, M., & Rutt, B. K. (2012). Hippocampal CA1 apical neuropil atrophy and memory performance in Alzheimer's disease.

- NeuroImage*, 63(1), 194–202. <http://doi.org/10.1016/j.neuroimage.2012.06.048>
- Kerchner, G. A., Hess, C. P., Hammond-Rosenbluth, K. E., Xu, D., Rabinovici, G. D., Kelley, D. A. C., et al. (2010). Hippocampal CA1 apical neuropil atrophy in mild Alzheimer disease visualized with 7-T MRI. *Neurology*, 75(15), 1381–1387. <http://doi.org/10.1212/WNL.0b013e3181f736a1>
- Khan, W., Westman, E., Jones, N., Wahlund, L.-O., Mecocci, P., Vellas, B., et al. (2015). Automated Hippocampal Subfield Measures as Predictors of Conversion from Mild Cognitive Impairment to Alzheimer's Disease in Two Independent Cohorts. *Brain Topography*, 28(5), 746–759. <http://doi.org/10.1007/s10548-014-0415-1>
- Killiany, R. J., Gomez-Isla, T., Moss, M., Kikinis, R., Sandor, T., Jolesz, F., et al. (2000). Use of structural magnetic resonance imaging to predict who will get Alzheimer's disease. *Annals of Neurology*, 47(4), 430–439.
- Killiany, R. J., Hyman, B. T., Gomez-Isla, T., Moss, M. B., Kikinis, R., Jolesz, F., et al. (2002). MRI measures of entorhinal cortex vs hippocampus in preclinical AD. *Neurology*, 58(8), 1188–1196. <http://doi.org/10.1212/WNL.58.8.1188>
- Kirwan, C. B., Jones, C. K., Miller, M. I., & Stark, C. E. L. (2007). High-resolution fMRI investigation of the medial temporal lobe. *Human Brain Mapping*, 28(10), 959–966. <http://doi.org/10.1002/hbm.20331>
- Konrad, C., Ukas, T., Nebel, C., Arolt, V., Toga, A. W., & Narr, K. L. (2009). Defining the human hippocampus in cerebral magnetic resonance images—An overview of current segmentation protocols. *NeuroImage*, 47(4), 1185–1195. <http://doi.org/10.1016/j.neuroimage.2009.05.019>
- Kuzniecky, R., Bilir, E., Gilliam, F., Faught, E., Martin, R., & Hugg, J. (1999). Quantitative MRI in temporal lobe epilepsy: evidence for fornix atrophy. *Neurology*, 53(3), 496–501.
- La Joie, R., Fouquet, M., Mézenge, F., Landeau, B., Villain, N., Mevel, K., et al. (2010). Differential effect of age on hippocampal subfields assessed using a new high-resolution 3T MR sequence. *NeuroImage*, 53(2), 506–514. <http://doi.org/10.1016/j.neuroimage.2010.06.024>
- La Joie, R., Perrotin, A., La Sayette, de, V., Egret, S., Doeuvre, L., Belliard, S., et al. (2013). Hippocampal subfield volumetry in mild cognitive impairment, Alzheimer's disease and semantic dementia. *NeuroImage. Clinical*, 3, 155–162. <http://doi.org/10.1016/j.nicl.2013.08.007>
- Lebel, C., Gee, M., Camicioli, R., Wieler, M., Martin, W., & Beaulieu, C. (2012). Diffusion tensor imaging

- of white matter tract evolution over the lifespan. *NeuroImage*, 60(1), 340–352.  
<http://doi.org/10.1016/j.neuroimage.2011.11.094>
- Lee, I., Rao, G., & Knierim, J. J. (2004). A Double Dissociation between Hippocampal Subfields. *Neuron*, 42(5), 803–815. <http://doi.org/10.1016/j.neuron.2004.05.010>
- Li, Y.-D., Dong, H.-B., Xie, G.-M., & Zhang, L.-J. (2013). Discriminative analysis of mild Alzheimer's disease and normal aging using volume of hippocampal subfields and hippocampal mean diffusivity: an in vivo magnetic resonance imaging study. *American Journal of Alzheimer's Disease and Other Dementias*, 28(6), 627–633. <http://doi.org/10.1177/1533317513494452>
- Libby, L. A., Ekstrom, A. D., Ragland, J. D., & Ranganath, C. (2012). Differential connectivity of perirhinal and parahippocampal cortices within human hippocampal subregions revealed by high-resolution functional imaging. *The Journal of Neuroscience : the Official Journal of the Society for Neuroscience*, 32(19), 6550–6560. <http://doi.org/10.1523/JNEUROSCI.3711-11.2012>
- Lim, H. K., Hong, S. C., Jung, W. S., Ahn, K. J., Won, W. Y., Hahn, C., et al. (2012). Automated hippocampal subfield segmentation in amnesic mild cognitive impairments. *Dementia and Geriatric Cognitive Disorders*, 33(5), 327–333. <http://doi.org/10.1159/000339588>
- Lim, H. K., Hong, S. C., Jung, W. S., Ahn, K. J., Won, W. Y., Hahn, C., et al. (2013). Automated segmentation of hippocampal subfields in drug-naïve patients with Alzheimer disease. *AJNR. American Journal of Neuroradiology*, 34(4), 747–751. <http://doi.org/10.3174/ajnr.A3293>
- Loken, C., Gruner, D., Groer, L., Peltier, R., Bunn, N., Craig, M., et al. (2010). SciNet: Lessons Learned from Building a Power-efficient Top-20 System and Data Centre. *Journal of Physics: Conference Series*, 256(1), 012026. <http://doi.org/10.1088/1742-6596/256/1/012026>
- MacLean, P. (1992). The limbic system concept. In M. R. Trimble & T. Bolwig (Eds.), *The Temporal Lobes and the Limbic System*. Petersfeild: Wrightson Biomedical Pub Limited.
- Mai, J. K., Majtanik, M., & Paxinos, G. (2015). *Atlas of the Human Brain*. Academic Press.
- Malykhin, N. V., Lebel, R. M., Coupland, N. J., Wilman, A. H., & Carter, R. (2010). In vivo quantification of hippocampal subfields using 4.7 T fast spin echo imaging. *NeuroImage*, 49(2), 1224–1230.  
<http://doi.org/10.1016/j.neuroimage.2009.09.042>
- Marcus, D. S., Wang, T. H., Parker, J., Csernansky, J. G., Morris, J. C., & Buckner, R. L. (2007). Open

- Access Series of Imaging Studies (OASIS): cross-sectional MRI data in young, middle aged, nondemented, and demented older adults. *Journal of Cognitive Neuroscience*, *19*(9), 1498–1507.  
<http://doi.org/10.1162/jocn.2007.19.9.1498>
- Metzler-Baddeley, C., O'Sullivan, M. J., Bells, S., Pasternak, O., & Jones, D. K. (2012). How and how not to correct for CSF-contamination in diffusion MRI. *NeuroImage*, *59*(2), 1394–1403.  
<http://doi.org/10.1016/j.neuroimage.2011.08.043>
- Mielke, M. M., Kozauer, N. A., Chan, K. C. G., George, M., Toroney, J., Zerrate, M., et al. (2009). Regionally-specific diffusion tensor imaging in mild cognitive impairment and Alzheimer's disease. *NeuroImage*, *46*(1), 47–55. <http://doi.org/10.1016/j.neuroimage.2009.01.054>
- Miller, M. I., Ratnanather, J. T., Tward, D. J., Brown, T., Lee, D. S., Ketcha, M., et al. (2015). Network Neurodegeneration in Alzheimer's Disease via MRI Based Shape Diffeomorphometry and High-Field Atlasing. *Frontiers in Bioengineering and Biotechnology*, *3*, 54.  
<http://doi.org/10.3389/fbioe.2015.00054>
- Mizutani, T., & Kasahara, M. (1995). Degeneration of the intrahippocampal routes of the perforant and alvear pathways in senile dementia of Alzheimer type. *Neuroscience Letters*, *184*(2), 141–144.  
[http://doi.org/10.1016/0304-3940\(94\)11190-T](http://doi.org/10.1016/0304-3940(94)11190-T)
- Moreno, H., Wu, W. E., Lee, T., Brickman, A., Mayeux, R., Brown, T. R., & Small, S. A. (2007). Imaging the Abeta-related neurotoxicity of Alzheimer disease. *Archives of Neurology*, *64*(10), 1467–1477.  
<http://doi.org/10.1001/archneur.64.10.1467>
- Morris, J. C. (1993). The Clinical Dementia Rating (CDR): current version and scoring rules. *Neurology*, *43*(11), 2412–2414.
- Mueller, S. G., & Weiner, M. W. (2009). Selective effect of age, Apo e4, and Alzheimer's disease on hippocampal subfields. *Hippocampus*, *19*(6), 558–564. <http://doi.org/10.1002/hipo.20614>
- Mueller, S. G., Chao, L. L., Berman, B., & Weiner, M. W. (2011). Evidence for functional specialization of hippocampal subfields detected by MR subfield volumetry on high resolution images at 4 T. *NeuroImage*, *56*(3), 851–857. <http://doi.org/10.1016/j.neuroimage.2011.03.028>
- Mueller, S. G., Schuff, N., Yaffe, K., Madison, C., Miller, B., & Weiner, M. W. (2010). Hippocampal atrophy patterns in mild cognitive impairment and Alzheimer's disease. *Human Brain Mapping*, *31*(9),

1339–1347. <http://doi.org/10.1002/hbm.20934>

- Mueller, S. G., Stables, L., Du, A. T., Schuff, N., Truran, D., Cashdollar, N., & Weiner, M. W. (2007). Measurement of hippocampal subfields and age-related changes with high resolution MRI at 4T. *Neurobiology of Aging*, 28(5), 719–726. <http://doi.org/10.1016/j.neurobiolaging.2006.03.007>
- Oishi, K., Mielke, M. M., Albert, M., Lyketsos, C. G., & Mori, S. (2012). The fornix sign: a potential sign for Alzheimer's disease based on diffusion tensor imaging. *Journal of Neuroimaging : Official Journal of the American Society of Neuroimaging*, 22(4), 365–374. <http://doi.org/10.1111/j.1552-6569.2011.00633.x>
- Olsen, R. K., Palombo, D. J., Rabin, J. S., Levine, B., Ryan, J. D., & Rosenbaum, R. S. (2013). Volumetric analysis of medial temporal lobe subregions in developmental amnesia using high-resolution magnetic resonance imaging. *Hippocampus*, 23(10), 855–860. <http://doi.org/10.1002/hipo.22153>
- Palombo, D. J., Amaral, R. S. C., Olsen, R. K., Müller, D. J., Todd, R. M., Anderson, A. K., & Levine, B. (2013). KIBRA polymorphism is associated with individual differences in hippocampal subregions: evidence from anatomical segmentation using high-resolution MRI. *The Journal of Neuroscience : the Official Journal of the Society for Neuroscience*, 33(32), 13088–13093. <http://doi.org/10.1523/JNEUROSCI.1406-13.2013>
- Pardoe, H. R., Kucharsky Hiess, R., & Kuzniecky, R. (2016). Motion and morphometry in clinical and nonclinical populations. *NeuroImage*, 135, 177–185. <http://doi.org/10.1016/j.neuroimage.2016.05.005>
- Parekh, M. B., Rutt, B. K., Purcell, R., Chen, Y., & Zeineh, M. M. (2015). Ultra-high resolution in-vivo 7.0T structural imaging of the human hippocampus reveals the endfolial pathway. *NeuroImage*, 112, 1–6. <http://doi.org/10.1016/j.neuroimage.2015.02.029>
- Pelletier, A., Periot, O., Dilharreguy, B., Hiba, B., Bordessoules, M., Pérès, K., et al. (2013). Structural hippocampal network alterations during healthy aging: a multi-modal MRI study. *Frontiers in Aging Neuroscience*, 5, 84. <http://doi.org/10.3389/fnagi.2013.00084>
- Pennanen, C., Kivipelto, M., Tuomainen, S., Hartikainen, P., Hänninen, T., Laakso, M. P., et al. (2004). Hippocampus and entorhinal cortex in mild cognitive impairment and early AD. *Neurobiology of Aging*, 25(3), 303–310. [http://doi.org/10.1016/S0197-4580\(03\)00084-8](http://doi.org/10.1016/S0197-4580(03)00084-8)
- Pereira, J. B., Valls-Pedret, C., Ros, E., Palacios, E., Falcón, C., Bargalló, N., et al. (2014). Regional

vulnerability of hippocampal subfields to aging measured by structural and diffusion MRI.

*Hippocampus*, 24(4), 403–414. <http://doi.org/10.1002/hipo.22234>

Pipitone, J., Park, M. T. M., Winterburn, J., Lett, T. A., Lerch, J. P., Pruessner, J. C., et al. (2014). Multi-atlas segmentation of the whole hippocampus and subfields using multiple automatically generated templates. *NeuroImage*, 101, 494–512. <http://doi.org/10.1016/j.neuroimage.2014.04.054>

Pluta, J., Yushkevich, P., Das, S., & Wolk, D. (2012). In vivo analysis of hippocampal subfield atrophy in mild cognitive impairment via semi-automatic segmentation of T2-weighted MRI. *Journal of Alzheimer's Disease : JAD*, 31(1), 85–99. <http://doi.org/10.3233/JAD-2012-111931>

Preston, A. R., Bornstein, A. M., Hutchinson, J. B., Gaare, M. E., Glover, G. H., & Wagner, A. D. (2010). High-resolution fMRI of content-sensitive subsequent memory responses in human medial temporal lobe. *Journal of Cognitive Neuroscience*, 22(1), 156–173. <http://doi.org/10.1162/jocn.2009.21195>

Pruessner, J. C., Köhler, S., Crane, J., Pruessner, M., Lord, C., Byrne, A., et al. (2002). Volumetry of temporopolar, perirhinal, entorhinal and parahippocampal cortex from high-resolution MR images: considering the variability of the collateral sulcus. *Cerebral Cortex (New York, N.Y. : 1991)*, 12(12), 1342–1353.

Pruessner, J. C., Li, L. M., Serles, W., Pruessner, M., Collins, D. L., Kabani, N., et al. (2000). Volumetry of hippocampus and amygdala with high-resolution MRI and three-dimensional analysis software: minimizing the discrepancies between laboratories. *Cerebral Cortex (New York, N.Y. : 1991)*, 10(4), 433–442.

Raz, N., Daugherty, A. M., Bender, A. R., Dahle, C. L., & Land, S. (2015). Volume of the hippocampal subfields in healthy adults: differential associations with age and a pro-inflammatory genetic variant. *Brain Structure & Function*, 220(5), 2663–2674. <http://doi.org/10.1007/s00429-014-0817-6>

Reuter, M., Tisdall, M. D., Qureshi, A., Buckner, R. L., van der Kouwe, A. J. W., & Fischl, B. (2015). Head motion during MRI acquisition reduces gray matter volume and thickness estimates. *NeuroImage*, 107, 107–115.

Sala, S., Agosta, F., Pagani, E., Copetti, M., Comi, G., & Filippi, M. (2012). Microstructural changes and atrophy in brain white matter tracts with aging. *Neurobiology of Aging*, 33(3), 488–498.e2. <http://doi.org/10.1016/j.neurobiolaging.2010.04.027>

- Salat, D. H., Chen, J. J., van der Kouwe, A. J., Greve, D. N., Fischl, B., & Rosas, H. D. (2011). Hippocampal degeneration is associated with temporal and limbic gray matter/white matter tissue contrast in Alzheimer's disease. *NeuroImage*, *54*(3), 1795–1802.  
<http://doi.org/10.1016/j.neuroimage.2010.10.034>
- Salat, D. H., Lee, S. Y., van der Kouwe, A. J., Greve, D. N., Fischl, B., & Rosas, H. D. (2009). Age-associated alterations in cortical gray and white matter signal intensity and gray to white matter contrast. *NeuroImage*, *48*(1), 21–28. <http://doi.org/10.1016/j.neuroimage.2009.06.074>
- Sasson, E., Doniger, G. M., Pasternak, O., Tarrasch, R., & Assaf, Y. (2013). White matter correlates of cognitive domains in normal aging with diffusion tensor imaging. *Frontiers in Neuroscience*, *7*, 32.  
<http://doi.org/10.3389/fnins.2013.00032>
- Scheff, S. W., Price, D. A., Schmitt, F. A., & Mufson, E. J. (2006). Hippocampal synaptic loss in early Alzheimer's disease and mild cognitive impairment. *Neurobiology of Aging*, *27*(10), 1372–1384.  
<http://doi.org/10.1016/j.neurobiolaging.2005.09.012>
- Schmahmann, J. D., Pandya, D. N., Wang, R., Dai, G., D'Arceuil, H. E., de Crespigny, A. J., & Wedeen, V. J. (2007). Association fibre pathways of the brain: parallel observations from diffusion spectrum imaging and autoradiography. *Brain : a Journal of Neurology*, *130*(Pt 3), 630–653.  
<http://doi.org/10.1093/brain/awl359>
- Shing, Y. L., Rodrigue, K. M., Kennedy, K. M., Fandakova, Y., Bodammer, N., Werkle-Bergner, M., et al. (2011). Hippocampal subfield volumes: age, vascular risk, and correlation with associative memory. *Frontiers in Aging Neuroscience*, *3*, 2. <http://doi.org/10.3389/fnagi.2011.00002>
- Sled, J. G., Zijdenbos, A. P., & Evans, A. C. (1998). A nonparametric method for automatic correction of intensity nonuniformity in MRI data. *IEEE Transactions on Medical Imaging*, *17*(1), 87–97.  
<http://doi.org/10.1109/42.668698>
- Small, S. A., Schobel, S. A., Buxton, R. B., Witter, M. P., & Barnes, C. A. (2011). A pathophysiological framework of hippocampal dysfunction in ageing and disease. *Nature Reviews. Neuroscience*, *12*(10), 585–601. <http://doi.org/10.1038/nrn3085>
- Sullivan, E. V., Rohlfing, T., & Pfefferbaum, A. (2010). Quantitative fiber tracking of lateral and interhemispheric white matter systems in normal aging: relations to timed performance. *Neurobiology*

*of Aging*, 31(3), 464–481. <http://doi.org/10.1016/j.neurobiolaging.2008.04.007>

Talairach, J., & Tournoux, P. (1988). *Co-planar Stereotaxic Atlas of the Human Brain*. George Thieme Verlag.

Tustison, N. J., Avants, B. B., Cook, P. A., Zheng, Y., Egan, A., Yushkevich, P. A., & Gee, J. C. (2010). N4ITK: improved N3 bias correction. *IEEE Transactions on Medical Imaging*, 29(6), 1310–1320. <http://doi.org/10.1109/TMI.2010.2046908>

Van Essen, D. C., Smith, S. M., Barch, D. M., Behrens, T. E. J., Yacoub, E., Ugurbil, K., WU-Minn HCP Consortium. (2013). The WU-Minn Human Connectome Project: an overview. *NeuroImage*, 80, 62–79. <http://doi.org/10.1016/j.neuroimage.2013.05.041>

Van Leemput, K., Bakkour, A., Benner, T., Wiggins, G., Wald, L. L., Augustinack, J., et al. (2009). Automated segmentation of hippocampal subfields from ultra-high resolution in vivo MRI. *Hippocampus*, 19(6), 549–557. <http://doi.org/10.1002/hipo.20615>

Varon, D., Loewenstein, D. A., Potter, E., & Greig, M. T. (2011). Minimal atrophy of the entorhinal cortex and hippocampus: progression of cognitive impairment. *Dementia and Geriatric*.

Vidal-Piñeiro, D., Walhovd, K. B., Storsve, A. B., Grydeland, H., Rohani, D. A., & Fjell, A. M. (2016). Accelerated longitudinal gray/white matter contrast decline in aging

Visser, P. J., Scheltens, P., Verhey, F. R. J., Ben Schmand, Launer, L. J., Jolles, J., & Jonker, C. (1999). Medial temporal lobe atrophy and memory dysfunction as predictors for dementia in subjects with mild cognitive impairment. *Journal of Neurology*, 246(6), 477–485. <http://doi.org/10.1007/s004150050387>

Voineskos, A. N., Winterburn, J. L., Felsky, D., Pipitone, J., Rajji, T. K., Mulsant, B. H., & Chakravarty, M. M. (2015). Hippocampal (subfield) volume and shape in relation to cognitive performance across the adult lifespan. *Human Brain Mapping*, 36(8), 3020–3037. <http://doi.org/10.1002/hbm.22825>

Wang, L., Swank, J. S., Glick, I. E., Gado, M. H., Miller, M. I., Morris, J. C., & Csernansky, J. G. (2003). Changes in hippocampal volume and shape across time distinguish dementia of the Alzheimer type from healthy aging. *NeuroImage*, 20(2), 667–682. [http://doi.org/10.1016/S1053-8119\(03\)00361-6](http://doi.org/10.1016/S1053-8119(03)00361-6)

Whitwell, J. L., Przybelski, S. A., Weigand, S. D., Knopman, D. S., Boeve, B. F., Petersen, R. C., & Jack, C. R. (2007). 3D maps from multiple MRI illustrate changing atrophy patterns as subjects progress

- from mild cognitive impairment to Alzheimer's disease. *Brain : a Journal of Neurology*, 130(Pt 7), 1777–1786. <http://doi.org/10.1093/brain/awm112>
- Winterburn, J. L., Pruessner, J. C., Chavez, S., Schira, M. M., Lobaugh, N. J., Voineskos, A. N., & Chakravarty, M. M. (2013). A novel in vivo atlas of human hippocampal subfields using high-resolution 3 T magnetic resonance imaging. *NeuroImage*, 74, 254–265. <http://doi.org/10.1016/j.neuroimage.2013.02.003>
- Wisse, L. E. M., Biessels, G. J., Heringa, S. M., Kuijf, H. J., Koek, D. H. L., Luijten, P. R., et al. (2014). Hippocampal subfield volumes at 7T in early Alzheimer's disease and normal aging. *Neurobiology of Aging*, 35(9), 2039–2045. <http://doi.org/10.1016/j.neurobiolaging.2014.02.021>
- Wisse, L. E. M., Gerritsen, L., Zwanenburg, J. J. M., Kuijf, H. J., Luijten, P. R., Biessels, G. J., & Geerlings, M. I. (2012). Subfields of the hippocampal formation at 7 T MRI: in vivo volumetric assessment. *NeuroImage*, 61(4), 1043–1049. <http://doi.org/10.1016/j.neuroimage.2012.03.023>
- Witter, M. P. (2007). The perforant path: projections from the entorhinal cortex to the dentate gyrus. In *The Dentate Gyrus: A Comprehensive Guide to Structure, Function, and Clinical Implications* (Vol. 163, pp. 43–61). Elsevier. [http://doi.org/10.1016/S0079-6123\(07\)63003-9](http://doi.org/10.1016/S0079-6123(07)63003-9)
- Yassa, M. A., Stark, S. M., Bakker, A., Albert, M. S., Gallagher, M., & Stark, C. E. L. (2010). High-resolution structural and functional MRI of hippocampal CA3 and dentate gyrus in patients with amnesic Mild Cognitive Impairment. *NeuroImage*, 51(3), 1242–1252. <http://doi.org/10.1016/j.neuroimage.2010.03.040>
- Yin, R.-H., Tan, L., Jiang, T., & Yu, J.-T. (2014). Prion-like Mechanisms in Alzheimer's Disease.
- Yushkevich, P. A., Amaral, R. S. C., Augustinack, J. C., Bender, A. R., Bernstein, J. D., Boccardi, M., et al. (2015a). Quantitative comparison of 21 protocols for labeling hippocampal subfields and parahippocampal subregions in in vivo MRI: towards a harmonized segmentation protocol. *NeuroImage*, 111, 526–541. <http://doi.org/10.1016/j.neuroimage.2015.01.004>
- Yushkevich, P. A., Avants, B. B., Pluta, J., Das, S., Minkoff, D., Mechanic-Hamilton, D., et al. (2009). A high-resolution computational atlas of the human hippocampus from postmortem magnetic resonance imaging at 9.4 T. *NeuroImage*, 44(2), 385–398. <http://doi.org/10.1016/j.neuroimage.2008.08.042>
- Yushkevich, P. A., Pluta, J. B., Wang, H., Xie, L., Ding, S.-L., Gertje, E. C., et al. (2015b). Automated

volumetry and regional thickness analysis of hippocampal subfields and medial temporal cortical structures in mild cognitive impairment. *Human Brain Mapping*, 36(1), 258–287.

<http://doi.org/10.1002/hbm.22627>

Yushkevich, P. A., Wang, H., Pluta, J., Das, S. R., Craige, C., Avants, B. B., et al. (2010). Nearly automatic segmentation of hippocampal subfields in in vivo focal T2-weighted MRI. *NeuroImage*, 53(4), 1208–1224. <http://doi.org/10.1016/j.neuroimage.2010.06.040>

Zahajszky, J., Dickey, C. C., McCarley, R. W., Fischer, I. A., Nestor, P., Kikinis, R., & Shenton, M. E. (2001). A quantitative MR measure of the fornix in schizophrenia. *Schizophrenia Research*, 47(1), 87–97.

Zahr, N. M., Rohlfing, T., Pfefferbaum, A., & Sullivan, E. V. (2009). Problem solving, working memory, and motor correlates of association and commissural fiber bundles in normal aging: a quantitative fiber tracking study. *NeuroImage*, 44(3), 1050–1062. <http://doi.org/10.1016/j.neuroimage.2008.09.046>

Zeineh, M. M., Holdsworth, S., Skare, S., Atlas, S. W., & Bammer, R. (2012). Ultra-high resolution diffusion tensor imaging of the microscopic pathways of the medial temporal lobe. *NeuroImage*, 62(3), 2065–2082. <http://doi.org/10.1016/j.neuroimage.2012.05.065>

Zheng, W., Chee, M. W. L., & Zagorodnov, V. (2009). Improvement of brain segmentation accuracy by optimizing non-uniformity correction using N3. *NeuroImage*, 48(1), 73–83. <http://doi.org/10.1016/j.neuroimage.2009.06.039>

Zhou, M., Zhang, F., Zhao, L., Qian, J., & Dong, C. (2015). Entorhinal cortex: a good biomarker of mild cognitive impairment and mild Alzheimer's disease. *Reviews in the Neurosciences*, 0(0). <http://doi.org/10.1515/revneuro-2015-0019>

Zhuang, L., Sachdev, P. S., Trollor, J. N., Reppermund, S., Kochan, N. A., Brodaty, H., & Wen, W. (2013). Microstructural white matter changes, not hippocampal atrophy, detect early amnesic mild cognitive impairment. *PloS One*, 8(3), e58887. <http://doi.org/10.1371/journal.pone.0058887>